공학박사 학위논문

Development of Plasma Information Based Advanced Process Controller (PI-APC) for Plasma Etch Processes

플라즈마 정보 기반의 식각공정용 고급 공정제어기 개발

2022년 8월

서울대학교 대학원

에너지시스템공학부

유 상 원

Development of Plasma Information Based Advanced Process Controller (PI-APC) for Plasma Etch Processes

지도 교수 김 곤 호

이 논문을 공학박사 학위논문으로 제출함
2022 년 8 월

서울대학교 대학원
에너지시스템공학부
유 상 원

유상원의 박사 학위논문을 인준함
2022 년 8 월

위 원 장 _____ 정 경 재 _____ (인)

부위원장 _____ 김 곤 호 _____ (인)

위 원 _____ 이 종 민 _____ (인)

위 원 _____ 김 용 진 _____ (인)

위 원 _____ 박 설 혜 _____ (인)

Abstract

Development of Plasma Information Based Advanced Process Controller (PI-APC) for Plasma Etch Processes

Sangwon Ryu

Department of Energy Systems Engineering

The Graduate School

Seoul National University

In plasma-assisted processes, it is essential to manage variation of process results due to changes in equipment conditions. As process scale shrinks, the effect of equipment conditions on the process yield, after the preventive maintenance (PM) or the deterioration of the process over time, is increasing. To manage the process drift, statistical process control (SPC) has been mainly used which is based on actual measurement of process results. However, a lot of time and cost consumption to measure process results make the measurement cycle as several hundred wafers. For more detailed process management, process measurement and control are required for each wafer. For this, virtual measurement (VM) technology of process results and R2R technology that revise recipes after each run have been developed. However, the equipment condition changes during the process due to the surface reaction between plasma and plasma-facing parts. Therefore, development of real-time process control technology, which control the process plasma while the process is going on, is inevitable for future process control.

In this thesis, PI-VM that observes changes in process results in real time during the process and real-time in-wafer controller named PI-APC,

equipment – plasma information (PI) variable – PI-VM 2 hierarchical loops controller, were developed for Si etch processes. The plasma-assisted process is divided into surface reaction between plasma and the process target and generation of plasma in the reactor. The process result that can be observed with PI-VM is the result of the surface reaction accumulated over time, and the PI variable that can be observed through optical emission spectroscopy (OES) is in dynamic equilibrium. Thus, the PI-APC should be the connection of equipment – PI controller and PI – PI-VM controller.

As Equipment – PI controller controls the generation of plasma, the control model could be developed based on a phenomenological dynamic model including power balance equations and particle balance equations. The gain of the controller represents the ratio of the generation reaction and the loss reaction of the PI variable, and the time constant of the controller represents the equipment dynamics as it has the slowest dynamics among the equipment, sensor, and plasma.

PI – PI-VM controller was developed based on the features and weightings of PI-VM developed with the stepwise variable selection based multiple linear regression (SVS-MLR) algorithm. As the PI-VM can evaluate the influence of PI variables on the process results, the control knob for process results could be determined from the features of PI-VM. Since the process result is the cumulative result of the surface reaction over time, the shrink horizon model predictive control method was used to convert the process result into PI variable which is in dynamic equilibrium. The effect of the other features was also expected with phenomenological model to linearize the control model.

The developed PI-APC could recognize the drift of process results by variation of chamber condition and adjusted the fluorine atom generation by the oxygen gas flow rate to enhance the etching reaction. PI-APC reduced the 12% variation in etch depth due to the first wafer effect to 0.5% variation through in-wafer control. Through the results of this thesis, it is shown that

the in-wafer controller, PI-APC, could manage the W2W process results variation. In addition, the nonlinearity of plasma process can be linearized and controlled by 2 loop controller based on a phenomenological model. Therefore, PI-APC, which describes various dynamic characteristics and non-linearities in the plasma process as a phenomenological model, is expected to be used in predictive maintenance (PdM), Tool-To-Tool Matching (TTTM) and process recipe optimization technology.

Keywords: plasma-information, virtual metrology (VM), advanced process control (APC), plasma etch, first wafer effect
Student Number: 2013-23183

Contents

List of Tables

List of Figures

Chapter 1. Introduction

In plasma-assisted processes, process shift after chamber preventative maintenance (PM) and process drift over time has been major issue. [1-4] The root cause of process drift is known as the variation of the chamber wall condition due to plasma-surface reactions. [1] As the surface loss and production probability of the particles on the chamber wall changed, particle densities in process plasma are also changed which results in process drift. Ramos et al. found out that the degree of dissociation of the Cl_2 plasma was strongly affected by the reactor wall condition. [2] As the Cl_2 plasma based Si etching process went on, the clean AlF wall was coated with SiOCl and the enhanced recombination rate of Cl atom made the degree of dissociation of Cl_2 doubled. Fukasawa et al. reported that the SiN etch rate by C_4F_8/Ar etching plasma was changed at most 50 % depending on the wall condition. [3] For the clean wall, etch rate was slower than the steady state wall condition as etchant species were consumed by the clean wall. As the process went on, the deposition of C-F polymer on the wall blocked the loss of etchant species on the wall so that the etch rate increased especially near the wall. Lee et al. observed critical dimension drift in a hardmask open etching process after wet cleaning of wall and over time. [4] The 3σ of critical dimension decreased just after the cleaning and gradually increased until the etching process repeated 15 times.

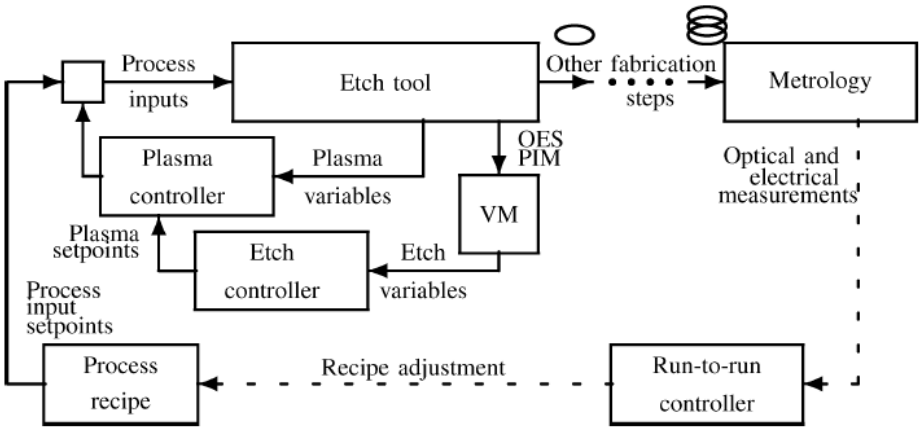

Figure 1.1 Possibilities of etch tool controller proposed by Ringwood et al. [5]

To resolve process drift issues, run-to-run (R2R) control scheme has been introduced. [4-6] As shown in dotted lines in Figure 1.1, R2R control is a form of discrete process control where the recipe could be modified between runs, so as to minimize process drift. [5] In R2R control, the black-box modeled relation between the recipes and the process results is trained and exponentially weighted moving average (EWMA) is used to modify process recipe for next run based on the process results for previous runs. Application of R2R control in semiconductor industry has mostly been lot-to-lot control [6] because of the high cost to measure process results directly. However, as the critical dimension shrinks wafer-to-wafer (W2W) control has become important and virtual metrology (VM) of process results, alternative to direct measurement, was essential to develop W2W controllers. [4] Lee et al. overcame critical dimension drift issue by implementing VM based W2W control scheme in plasma etching. The uniformity of CD across the wafer was

predicted by VM and the gas flow rate between center and edge area in a showerhead was controlled for every wafer based on the VM results for previous runs.

However, the source of process drift, variation of chamber wall condition, changes during the process and it is inevitable to implement real-time control scheme which adjust recipes during the processes as drawn in Figure 1.1, not between runs, to compensate process drift for more sophisticated processes. Real-time controller for process plasmas has been presented in a few publications. [6-8] Keville et al. demonstrated real time feedback controller for electron density in a capacitively coupled argon plasma. [7] Their controller adjusted RF power to keep the electron density at set value when a leak of helium into the chamber was acting as a disturbance. Klimecky et al. showed that the etch depth of poly-Si increased for each wafer after the C_2F_6 wall cleaning. [8] They adjusted the transformer coupled plasma (TCP) coil power to compensate the increase of electron density in Cl_2 etching plasma monitored by a microwave cavity resonance sensor. Lynn et al. changed the ground impedance acting as disturbance in He/SF_6 etch plasma. [6] To mitigate the change of electron density by the variation of the ground impedance, they controlled RF power to keep electron density at the set value. In these real time controllers, W2W plasma variation was controlled during the runs which was started with same recipes regardless of chamber conditions.

The W2W controllers proposed by previous researchers monitored process results by VM and used data driven black-box control model between process

recipe and process results. Meanwhile, the real-time controllers proposed by previous researchers were equipment – plasma controllers which did not monitor and control process results directly. To develop real-time process controller, real-time monitoring of process results and bridging the relation between equipment and process results with plasma parameters are needed. In this paper, the challenges were solved by using virtual metrology based on plasma information (PI-VM) which was introduced by Park et al. [9] PI-VM model used plasma information (PI) variables extracted from analysis on raw sensor data in additional to equipment and sensor data that are used in traditional VM. As the PI variables provide information that is not available in equipment and raw sensor data, the PI-VM showed higher prediction accuracy than conventional VM methods. [9-11] Moreover, the input data of PI-VM are all available in real-time which means the PI-VM also could monitor process drift in real-time. From recent research on PI-VM by Jang et al., the PI-VM model described the process results as a linear summation of weighted features which could be used as control knobs connecting equipment recipe and process results. [11] Therefore, the PI-VM model could provide high accuracy real-time monitoring method for process results and control knobs among the features of the linearized model.

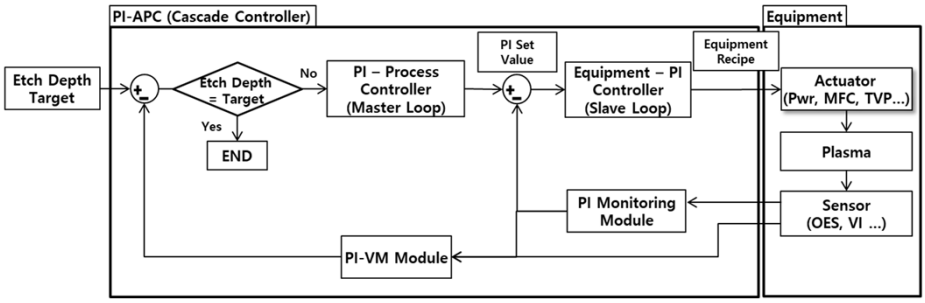

Figure 1.2 Block diagram of PI-APC, Equipment – PI – PI-VM, Controller

In this thesis, the real-time controller which directly controls process results is developed for the first time as form of Equipment – PI – PI-VM 2 loop controller, named PI-APC, to compensate the W2W process drift by in-wafer controllers. As shown in Figure 1.2, PI-APC consists of two control loops; an outer controller and an inner controller. The output of the outer controller is delivered to the slave controller as setpoint. This connection of the outer controller and inner controller is essential as the control target of outer loop is time-integrated surface reaction while the control target of inner loop is plasma information variable which is in dynamic equilibrium. The drift of process results monitored by PI-VM model could be controlled by adjusting PI variables which is selected among the features of the PI-VM model as the plasma-surface interaction dominates the process results. Then the required amount of PI variable was calculated by the outer controller considering time-varying effect of disturbances and transferred to the Equipment – PI controller. As the equipment recipe dominates generation of the plasma, the inner controller would calculate new equipment recipe to satisfy the delivered setpoint of PI. The PI-APC will adjust process recipe during the processes

from the same initial values and compensate the W2W process drift regardless of chamber wall conditions. The remainder of this paper is organized as follow; The details on equipment, process and PI monitoring methods are described in chapter 2I. Chapter 3 contains development and analysis of the Equipment – PI controller. In chapter 4, the development and PI-VM and PI – PI-VM outer controller and demonstration of the cascade controller are described and discussed. The conclusion and future works are covered in chapter V.

Chapter 2. Experimental Details

2.1 Equipment Details

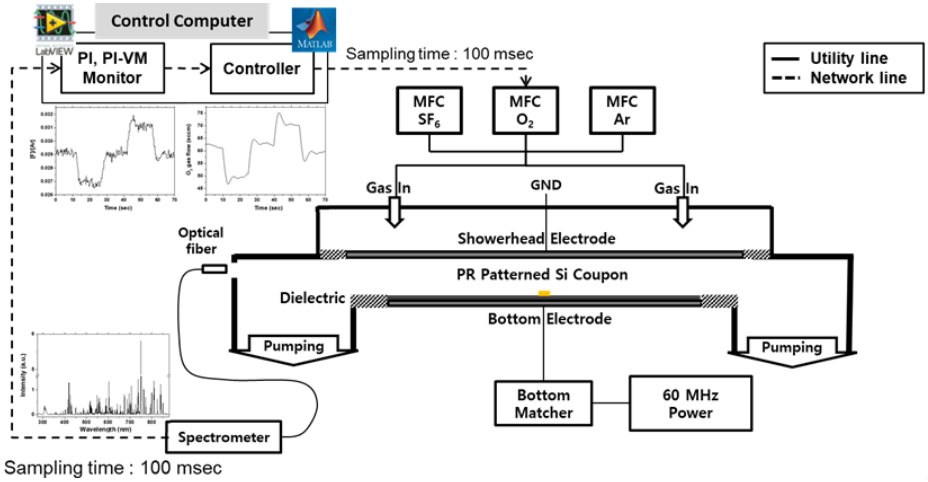

Figure 2.1 Schematic of etch process equipment and control system

A schematic of a narrow gap capacitively coupled plasma etch system, which is common in semiconductor etching processes, is shown in Figure 2.1. A 60 MHz power generator delivered RF power to the bottom electrode through an automatic matching network to generate etching plasma, while the top electrode was connected to ground. SF_6, O_2, and Ar gases were supplied to the reactor through the showerhead of the top electrode and the flow rates were adjusted by mass flow controllers (MFC). The reactor pressure was maintained at 20 mTorr by the throttle valve between the reactor and the turbomolecular pump. A spectrometer (Avaspec ULS2048L) was set to measure volume and time integrated emission spectra of the plasma through

an optical fiber observing radial center of the reactor. The actuators and spectrometer were connected to the control computer via UDP data transfer protocol. The control computer, which received data from the actuators and sensors, calculated PI, PI-VM and control moves and sent the control moves to the actuators. As the control computer request and got the data from actuators, sensors, PI module and PI-VM module for every 100 msec, all data are synched and logged for the 100 msec sampling time. The algorithms for PI and PI-VM monitoring modules and control modules were developed on LABVIEW and MATLAB SIMULINK environment.

2.2 Plasma Information (PI) monitoring method

PI variables offer useful information on the process plasma that could not be provided by equipment and raw sensor data. PI variables include thermal equilibrium state of plasma and density of particles. In this research, electron temperature and densities of electrons and radicals were monitored in real-time by analyzing the optical emission spectrum of the plasma.

2.2.1 Electron density

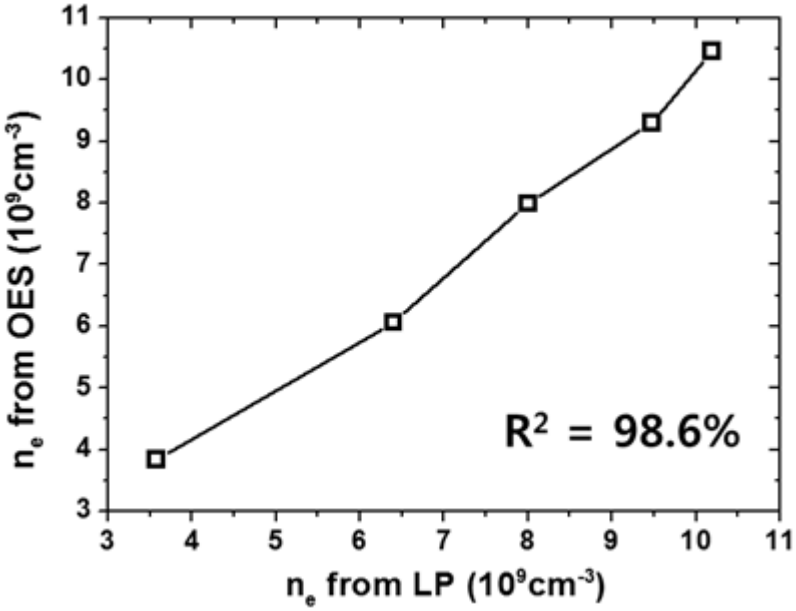

Figure 2.2 Electron density measured from Langmuir probe analysis and optical emission spectroscopy method.

$$I_X = n_e n_X Q_{exc} = n_e n_X \int_{E_{thr}}^{\infty} \sigma(\varepsilon)\sqrt{\varepsilon/2m_e}\, f(\varepsilon) d\varepsilon \qquad (1)$$

For low temperature and low pressure plasmas like etch plasma for semiconductor manufacturing, corona equilibrium could be used to analyze the intensity of emission from excited species in plasma. Following to corona equilibrium model, an emission intensity from an excited specie could be described as Equation (1). [12] The I_x, is the emission intensity, n_e, is the density of electrons, n_x, is the density of particle X in ground state, and Q_{exc}, is the electron impact excitation rate from the ground state of X. The Q_{exc} is determined by atomic characteristics of particle X, σ, and the thermal

equilibrium state of electrons, $f(\varepsilon)$. Assuming that the electron temperature is not changed much, the electron density could be monitored by the ratio of the emission intensity and the ground state Ar density. The 750.4 nm emission line which is deexcited from 2p1 state of Ar to 1s2 state of Ar was selected to monitor electron density as the electron impact excitation rate from ground state to 2p1 state is dominant compared to the excitation rate from metastable states of Ar which means corona equilibrium model fits well for the Ar 750.4 nm emission line.

To confirm the linear relation and calibrate the intensity of the light emission to electron density, comparison between the selected line emission intensity with the spectrometer and electron density with a Langmuir probe varying the RF power was done. As it is shown in Figure 2.2, the intensity of the light emission and the electron density have linear relation with $R^2 = 0.986$, and by calibrating the intensity to the electron density, monitoring of the electron density in-situ and real-time was available.

2.2.2 Electron temperature

The thermal equilibrium state of electrons could be represented as electron energy distribution function (EEDF). As the EEDF dominates the generation rates of particles in plasma, monitoring EEDF could be significant to figure out the density ratio of radicals and ions in plasma. The EEDFs in plasmas are generally classified as bi-Maxwellian, Maxwellian and Druyvestyen depending on the deviation of high energy electron population from that of Maxwellian EEDF. [13] The generalized form of the EEDF, $f_e(E)$, in plasma

could be described as

$$f_e\left(E\right)=c_1T_x^{-3/2}\sqrt{E}e^{-c_2\left(E/T_x\right)^x} \tag{2}$$

where c_1 and c_2 are function of the effective electron temperature, T_{eff}, and the shape factor, x. [13]

$$c_1=x\left(\frac{3}{2}kT_{eff}\right)^{-3/2}\frac{\left[\Gamma\left(5/2x\right)\right]^{3/2}}{\left[\Gamma\left(5/2x\right)\right]^{5/2}} \tag{3}$$

$$c_2=\left(\frac{3}{2}kT_{eff}\right)^{-x}\left[\frac{\Gamma\left(5/2x\right)}{\Gamma\left(5/2x\right)}\right]^x \tag{4}$$

Monitoring T_{eff} and x could provide information on the EEDF of the plasma, as T_{eff} represents averaged thermal energy of electrons in plasma and x represents the relative population of high energy electron. S. Park et al., derived the PI parameters from the balance of electron impact excitation and spontaneous emission of excited Ar species; collisional radiative model (CRM). [14]

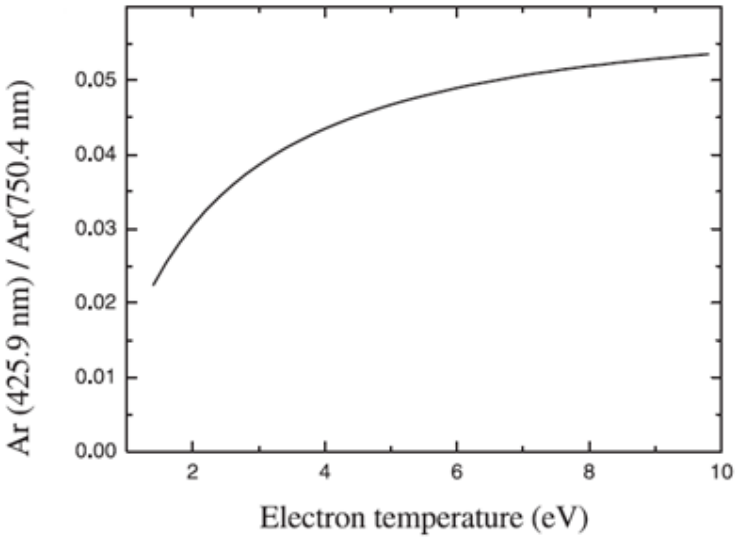

Figure 2.3 Ar line intensity ratio, 425.9 nm and 750.4 nm and electron temperature [15]

As the emission intensity is function of electron density, ground state Ar density and the excitation rate, the ratio of two emission intensity represented the ratio of excitation rates which is determined by the thermal equilibrium state of electrons. In this thesis, for fast sampling speed (100 msec), the simple method proposed by Boffard et al. was used, which assumed Maxwellian EEDF and monitored T_{eff} by the ratio of 425.9 nm and 750.4 nm lines from Ar. [15]

2.2.3 Radical density

$$\frac{I_A}{I_X} = \frac{n_e n_A Q_{exc,A}}{n_e n_X Q_{exc,B}} = C_A \frac{n_A}{n_X} \tag{5}$$

To monitor the densities of radicals in the etch plasma, optical emission actinometry is generally used. As described in Equation (5), the actinometry is

a method to monitor density of certain particle in interest by the ratio of the emission intensity of the particle and that of reference particle, generally noble gas. In $SF_6/O_2/Ar$ etch processes after the wall cleaning, fluorine, oxygen and hydrogen atoms would be major atoms as fluorine and oxygen contributes to etch reactions and hydrogen reflects the wall condition. By using 750.4 nm emission line from Ar as the reference, 703.7 nm, 777.4 nm and 656.3 nm emission lines were used to monitor fluorine, oxygen and hydrogen atom densities. The selected lines are strong and distinguishable emission lines from the emission spectrum. The actinometric coefficients, C_A, for fluorine and oxygen published by Lopaev et al. [16] and the actinometric coefficient of hydrogen obtained by Skoro et al. [17] were used to monitor radical densities in the $SF_6/O_2/Ar$ etch plasma.

2.3 Process details

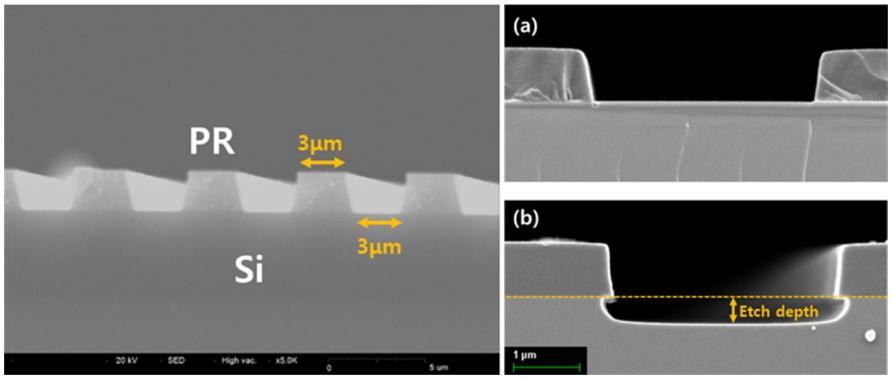

Figure 2.4 SEM image of PR patterned Si target before etch (a) and after etch (b).

The target process was etching of Si wafer coupons covered with 3 μm line spacing photoresist (DPR-i5500, 4000 rpm, 1 μm thickness). The scanning

electron microscope (SEM) image of the cross-section of the coupon is shown in Figure 2.4. In narrow gap VHF CCP, the uniformity of process plasma and process results is affected by not only gas diffusion property but also plasma series resonance and standing wave effect. However, in this thesis, the process plasma and the process results are assumed to be in 0-D uniformity and therefore the Si coupons, placed on the radial center of the dummy wafer on the bottom electrode, represents the etching process on entire wafer. To etch Si coupons, 20 mTorr mixed gas of 120 sccm SF_6, 0~100 sccm O_2 and 50 sccm Ar were discharged by 900 W of 60 MHz power for 1 minute. SF_6 provided etchants, fluorine atoms, from dissociation reactions and O_2 helped dissociation of SF_6 and Ar provided electrons and positive ions by ionization reactions. The 60 MHz power induced at bottom electrode generated plasma by stochastic heating of electrons and accelerated ions by self-bias to enhance the vertical etch of the coupon. The operating condition and the range of PI variables for the experiments are written in table 2.1.

Table 2.1 Operating condition and PI variables for experiments.

Pressure (mTorr)	**Ar (sccm)**	**O_2 (sccm)**	**SF_6 (sccm)**	**60 MHz Power (W)**
20	50	0 ~ 100	120	900
n_e ($10^9 cm^{-3}$)	**T_e (eV)**	**n_F ($10^{12} cm^{-3}$)**	**n_O ($10^{12} cm^{-3}$)**	**Etch time (sec)**
5.7 ~ 6.2	3.2 ~ 3.6	5.5 ~ 12	2.8 ~ 30	60

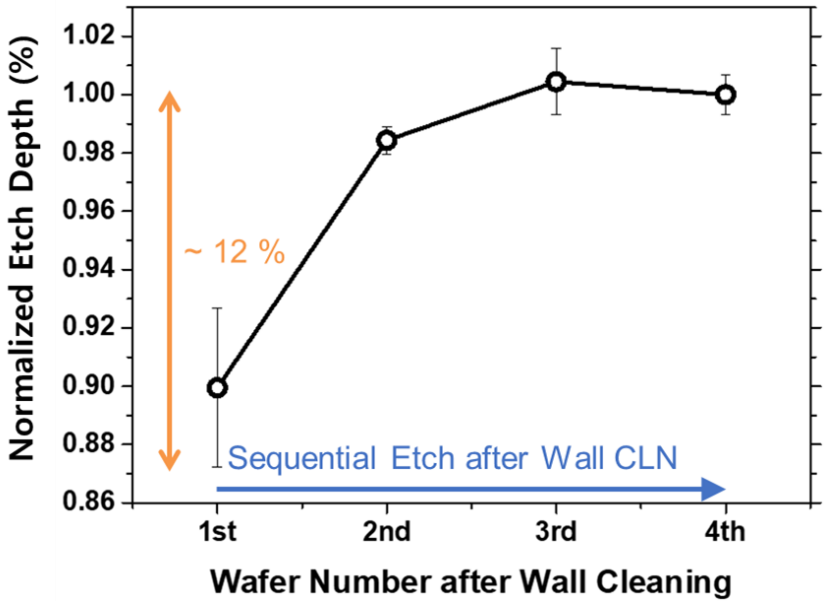

Figure 2.5 Etch depth measured with SEM image analysis for sequential etches after wall cleaning with ethanol.

As referred in chapter 1, reproducibility of process results is degraded just after the PM and as process repeated for several lots. To simulate drift of process results for several lots, load lock system is inevitable and hundreds of wafers should be etched, which is not available in laboratory system. Thus, in this thesis, process variation after PM event is selected as control target. PM were done by wiping the plasma facing materials with ethanol to restore the chamber wall condition into initial state. To confirm the effect of PM on etch depth of Si, 4 sequential etch processes were done after the PM and the etch depth was measured by SEM analysis. As shown in Figure 2.5, the etch depth of initial two wafers were shallower than that of later two wafers, maximum 12 %, and the variation of etch depth decreases until the third etch process.

This etch depth variation after the PM event is called as “first wafer effect” [8] and compensate the first wafer effect with PI-APC is the control target of this thesis.

Chapter 3. Develop RF Power – Electron Density Controller

In this chapter, development of Equipment – PI control based on phenomenological model is described. The Equipment – PI controller, inner loop controller of PI-APC, adjust plasma generation reaction by process recipe to achieve target PI value which would be provided by PI – PI-VM controller. As the controller is based on dynamic equilibrium of the plasma, the Equipment – PI controller could be developed by phenomenological model based model predictive controller (MPC) where phenomenological model includes plasma physics and chemistry and gas phase kinetics.

3.1 Phenomenological model based dynamic model

In plasma-assisted processes, particle flux to the surface is key to control process results. The particle flux to the surface is mainly determined by electron density as the particle generation in plasma is done by electron impact inelastic collisions. Therefore, electron density was selected as controlled variable in this chapter. The manipulated variable was selected as 60 MHz power as it is well known that the generation of electrons is mainly enhanced by electron heating by RF power. To establish the control model that describes dynamic relation between RF power and electron density, power balance equation by Liebermann [18] was rearranged.

$$\frac{dU_e}{dt} = \frac{d}{dt}\left(\frac{3}{2}n_e kT_e\right) = \frac{P_e}{V} - e\varepsilon_T K_{iz} n_e n_g \tag{6}$$

Equation (6) describes the balance between the electron heating power and energy loss by electrons in plasma. U_e is electron energy density, n_e is electron density, k is boltzman constant, T_e is electron temperature, P_e, power absorbed by electrons in plasma, V is the volume of the plasma, e is electron charge, ε_T is energy lost per electron-ion pair leaving the plasma, K_{iz} is ionization rate, and n_g is neutral gas density. For initial steady state, equation (6) and the electron density at initial state could be written as below.

$$\frac{P_e}{V} = e\varepsilon_T K_{iz} n_e n_g \tag{7}$$

$$n_e(t=0) = n_{e0} = \frac{P_e}{e\varepsilon_T K_{iz} n_g V} \tag{8}$$

When the RF power was adjusted to change electron heating power, ΔP_e, and wait for steady state, the equation (6) and the electron density at final state could be written as below.

$$\frac{dU_e}{dt} = \frac{P_e + \Delta P_e}{V} - e\varepsilon_T K_{iz} n_e n_g \tag{9}$$

$$n_e\left(t \to \infty\right) = n_{e\infty} = \frac{P_e + \Delta P_e}{e\varepsilon_T K_{iz} n_g V} \tag{10}$$

For the time between equation (8) and (10), equation (6) would be written as below.

$$\frac{d}{dt}\left(\frac{3}{2}kT_e n_e\right) = \frac{P_e + \Delta P_e}{V} - e\varepsilon_T K_{iz} n_e n_g \tag{11}$$

Assuming that the electron temperature is independent of power variation,

equation (11) could be organized as below.

$$\frac{dn_e}{dt} = \frac{P_e + \Delta P_e}{V}\frac{2}{3kT_e} - e\varepsilon_T K_{iz} n_g \frac{2}{3kT_e} n_e \tag{12}$$

Solving the equation (12) with initial and final condition from equation (8) and (10) results in time transient change of electron density when the RF power is changed.

$$n_e(t) = (n_{e0} - n_{e\infty}) e^{\frac{-2e\varepsilon_T K_{iz} n_g}{3kT_e} t} + n_{e\infty} \tag{13}$$

$$\Delta n_e = n_{e\infty} - n_e(t) = \left(\frac{\Delta P_e}{e\varepsilon_T K_{iz} n_g V} \right) e^{\frac{-2e\varepsilon_T K_{iz} n_g}{3kT_e} t} \tag{14}$$

Laplace transformation of equation (14) results in first order transfer function which is common as linear control model.

$$\Delta n_e = \frac{G\eta}{\tau s + 1} \Delta P_{RF} \ \ (where \ \ G = 1/e\varepsilon_T K_{iz} n_g V, \ \tau = 3kT_e / 2e\varepsilon_T K_{iz} n_g) \tag{15}$$

The linear gain, G, in equation (15) represents energy loss by electrons in plasma, η is power transfer efficiency from RF generator to electrons and the time constant, τ, means energy relaxation time of heated electrons. As electrons in plasma lost their energy through surfaces and collisions with neutral gas species and ions, the gain could be described as below.

$$G^{-1} = e\varepsilon_c K_{iz} n_g V + e(\varepsilon_e + \varepsilon_i) u_B^* A_{eff} \tag{16}$$

The first term of the right-hand side of equation (16) is collisional energy loss of electron and it was calculated by integrating major electron impact

cross-sections, σ, of Ar [19] and SF_6 [20] with electron energy distribution function (EEDF) measured from OES following to Park et al. [9].

$$e\varepsilon_c K_{iz} n_g V = \sum_i e\varepsilon_{c,i} n_i V \int \sigma(\varepsilon)\sqrt{2\varepsilon / m_e}\, f(\varepsilon)\, d\varepsilon \tag{17}$$

The second term of right-hand side of equation (17) is surface energy loss of electrons and ions, where ε_e and ε_i are mean kinetic of electrons and ions, u_B* is bohm velocity for weakly electro-negative plasma [21] and A_{eff} is effective particle loss area for intermediate pressure [18]. The electro-negativity of the plasma, which is defined as the ratio of negative ions to electrons, was measured as 0.8 from Langmuir probe signals [22] assuming that the majority of positive ion is Ar^+ and the majority of negative ion is SF_6^- as they have the highest generation rates in our experimental setup. Summation of collisional energy loss and surface energy loss results in the linear gain as 2.63 x $10^8 cm^{-3}/W$.

$$\eta = \left(P_{stoch.} + P_{ohm.}\right) / P_{RF} \tag{18}$$

$$P_{stoch.} = 0.45\sqrt{m / e}\,\varepsilon\omega^2 T_e^{1/2} V_{RF} A \tag{19}$$

$$P_{ohm.} = 1.73 \frac{m}{2e} \frac{n_s}{n_0} \varepsilon\omega^2 T_e^{1/2} V_{RF} dA \tag{20}$$

The power transfer efficiency, η, could be estimated from the ratio of electron heating power, $P_{stoch.}$ and $P_{ohm.}$, and the output power from RF generator, P_{RF} as written in equation (18). In low pressure very high frequency (VHF) capacitively coupled plasma (CCP), electrons are mainly heated by stochastic heating. Equation (19) is stochastic heating from

Liebermann et al., [18] where m is mass of electron, e is electric charge, ε is permittivity, ω is angular frequency of RF power, V_{RF} is voltage across a sheath and A is area of electrode. Equation (20) is ohmic heating from Liebermann et al., [18] where n_s is electron density at sheath boundary, n_0 is electron density at bulk plasma, d is the gap between electrodes. The voltage measured between the electrode and the matcher was used to calculate stochastic heating power and ohmic heating power and the power transfer efficiency was calculated as 0.57 in our experimental setup.

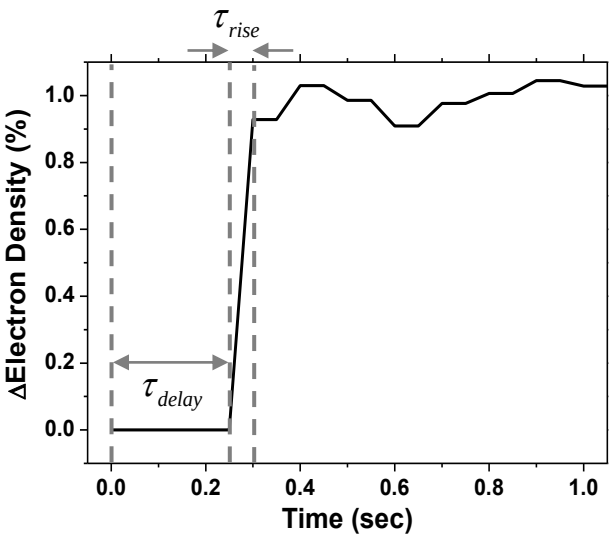

Figure 3.1 Step response of electron density when RF power was changed

The time constant in equation (15), τ, could be calculated by the ratio of the linear gain and electron temperature and it was order of hundred microseconds which is too fast to be detected by electron density monitoring method described in section 2.2.1. Therefore, the electrons could be assumed

to react instantly when the input RF power was changed. However, the system applying RF power to the reactor takes time to deliver set-point from the control computer to the RF generator through LAN cable, adjust power to set-point inside the RF generator and run motors to match impedance inside the matching network. In Figure 3.1, the characteristic time of RF system was measured from the log data of step power change sequence and the delay time, τ_d, was 0.25 sec and the rise time, τ_r, was 0.05 sec. Therefore, the control model could be written as below which consists of both plasma physics model and dynamics of hardware system.

$$\Delta n_e = \frac{G\eta}{\tau_r s + 1} e^{-\tau_d s} \Delta P_{RF} \tag{21}$$

3.2 Model Predictive Control

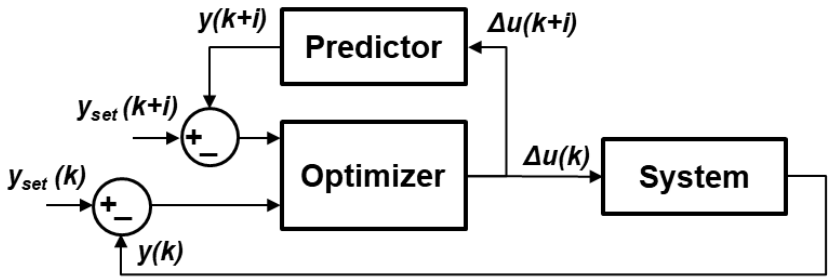

Figure 3.2 Block diagram of model predictive controller

$$y(k+j) = \sum_{i=1}^{j} S_i u'(k+j-i) + \sum_{i=j+1}^{n-1} S_i u'(k+j-i) + S_n u'(k+j-n) \tag{22}$$

Model predictive control (MPC) is an advanced control technique that predicts future moves of the outputs and calculate optimized control moves.

[24] Basic structure of MPC is drawn in Figure 3.2. Predictor contains an internal model that describes dynamics between input and output. Equation (22) describes how predictor calculates the future move of output, *y(k+j)*, with internal model S_i. The first term of the right-hand side of equation (22) is effect of current and future control actions to the output and the second term of right-hand side of equation (22) is effect of past control actions to the output. The internal model of the controller is developed in section 3.1 as equation (21). Therefore, parameters in objective function should be determined to complete the MPC for RF power – electron density.

$$J\left(z_k\right)=\sum_{i=1}^{P} e_y^T\left(k+i\right)Qe_y\left(k+i\right)+\sum_{i=1}^{M} u'^T\left(k+i\right)Ru'\left(k+i\right) \tag{23}$$

The optimizer calculates control moves to minimize objective function, equation (23), where *Q* is weighting for error of controlled variable, e_y, *R* is weighting for change of manipulated variable, *u'*, *P* is prediction horizon and *M* is control horizon. When *Q* is higher than *R*, the controller considers error of controlled variable is more important than change of manipulated variable which results in aggressive control moves. When *R* is higher than *Q*, the controller shows sluggish control moves as change of manipulated variable is more significant than error of controlled variable.

$$\begin{aligned} e_y\left(k+i\right) &= y_{set}\left(k+i\right)-\hat{y}\left(k+i\right) \\ &= y_{set}\left(k+i\right)-\sum_{j=1}^{i} S_j u'\left(k+i-j\right) \\ &\quad +\sum_{j=i+1}^{n-1} S_j u'\left(k+i-j\right)+S_n u'\left(k+i-n\right) \end{aligned} \tag{24}$$

As the control model is established, the error of controlled variable could be formulated from set-point of controlled variable, y_{set}, trajectory of controlled variable, $\hat{y}$, and moves of manipulated variable, u', where S_i is step-response function based on the linear control model, equation (24). Substituting e_y in equation (23) as equation (24) make the objective function as a function of moves of manipulated variable. Therefore, the control moves to minimize objection function could solved be as quadratic program (QP) problem. In this paper, QP solvers produced by Model Predictive Control Toolbox™ in MATLAB Simulink® was used to run MPC.

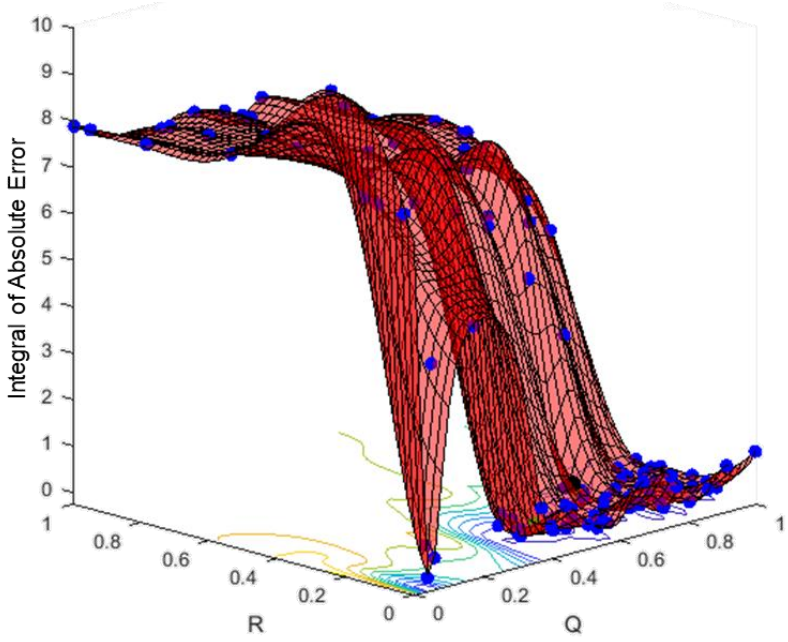

Figure 3.3 Integral of Absolute Error for simulated set-point tracking test with randomly selected *Q*, *R* combinations.

$$IAE = \int_0^{\tau} \left| n_{e,set}(t) - n_e(t) \right| dt \tag{25}$$

The integral of the absolute error (IAE), equation (25), could be an index for performance of the controller. [23] To determine the combination of *Q* and *R* with best control performance, the simulation of set-point tracking tests with random *Q* and *R* combination was conducted for 100 times. The combination of *Q* and *R* with the least IAE of controlled variable was selected. For low *R* and high *Q*, the integral squared error was small and it could be explained by the characteristic of controller system. As mentioned earlier, electrons react much faster than the RF power delivery system. Therefore, the controller doesn't have to hesitate to vary RF power which results in small penalty on change of manipulated variable, low *R*, and high penalty on error of controlled variable, high *Q*. The selected *Q* and *R* showed best performance in set-point tracking test while the combination of lower *R* or higher *Q* results in large oscillation on control action.

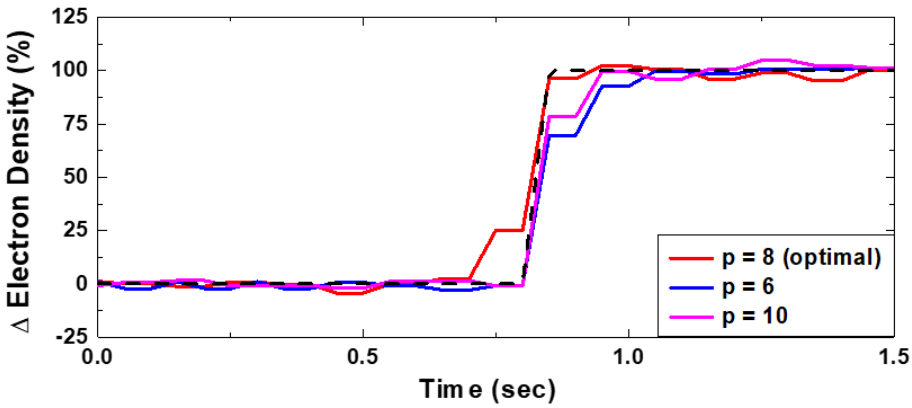

Figure 3.4 Set-point tracking tests for different prediction horizons.

The control horizon and prediction horizon were set following to rules of

thumb suggested by Seborg [23]. The control horizon would be over the third of the model horizon and under the half of the model horizon where the model horizon is defined as the settling time over the sampling time. The prediction horizon is set to the sum of the control horizon and the model horizon to consider the effect of last move of manipulated variable. As the sampling time of the system was 50 msec and the settling time of electron density when RF power was changed was 300 msec, the model horizon was 6, the control horizon was set to 3 and the prediction horizon was set to 8. It is confirmed that the rule of thumbs works for the RF power – electron density controller by comparing IAE of different prediction horizons in step response tests which is drawn in Figure 3.4. For the optimal case, where the prediction horizon was set to 8, the IAE of the controller was the smallest, $3.12 \times 10^{10} cm^{-3}$, while in other cases the IAE was $3.25 \times 10^{10} cm^{-3}$ and $3.21 \times 10^{10} cm^{-3}$.

3.3 Set-point Tracking Test

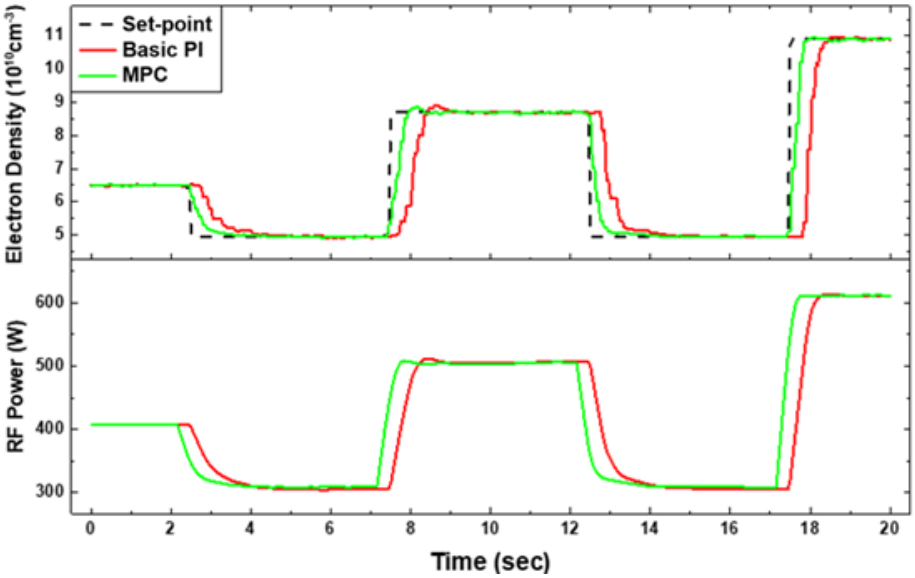

Figure 3.5. Set-point tracking tests for basic PI controller and the phenomenological model based MPC.

To confirm the performance of the phenomenological model based predictive controller, comparison with basic PI controller was conducted. A set-point tracking test with sequential step change in the reference experimental condition was done for both PI controller and MPC. The parameters of the PI controller were tuned by internal model control (IMC) method proposed by Chien and Fruehauf [24]. Figure 3.5 is the set-point tracking test results for both control techniques. For all step changes, the PI controller reached set-point of electron density 0.5 sec slower than the MPC. The performance of the controllers was quantified as IAE. The IAE of PI was 8.89 x $10^{10}cm^{-3}$ which is 3 times larger than the IAE of MPC, 3.12 x $10^{10}cm^{-3}$.

As the MPC knows the delay time and the rise time of the RF delivery system, MPC adjusted RF power earlier to satisfy electron density set-point quickly following to the objective function and the control model while the simple PI couldn't expect the future moves of the system and only compensates error at present time through the control parameters. For plasma-assisted processes, the time characteristics of actuators are generally slower than that of plasma parameters. Moreover, each actuators and plasma parameters has their own time characteristics which makes MPC more efficient than traditional PI controllers.

Chapter 4. Develop PI-APC for First Wafer Effect

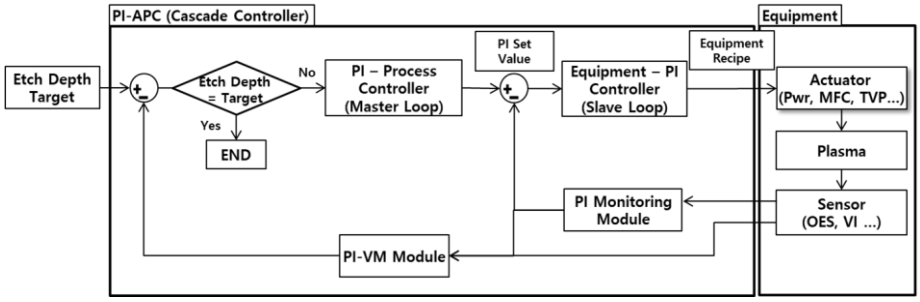

Figure 4.1. Block diagram of PI-APC, Equipment – PI – PI-VM 2 loop controller.

In this chapter, development of PI-APC to compensate the W2W etch depth variation after the PM referred in section 2.3 by in-wafer control is described. To monitor the W2W etch depth variation and in-wafer etch rate variation, PI-VM was developed first. Based on the analysis on the features and weightings of the PI-VM, manipulated variable for outer loop, same as controlled variable for inner loop, was selected as fluorine atom density. The inner loop controller was developed following the sequences in chapter 3, but in this case, non-linearity was considered. The outer loop controller was developed by shrinking horizon model predictive controller (SHMPC) as the outer loop controller should convert time integrated surface reaction into dynamic equilibrium state of plasma of PI-APC. The operation window of PI-APC was tested by adjust etch time and finally the PI-APC was adopted to compensate W2W etch depth variation as steady by in-wafer control regardless of wall

conditions.

4.1 Develop PI-VM for Etch Depth

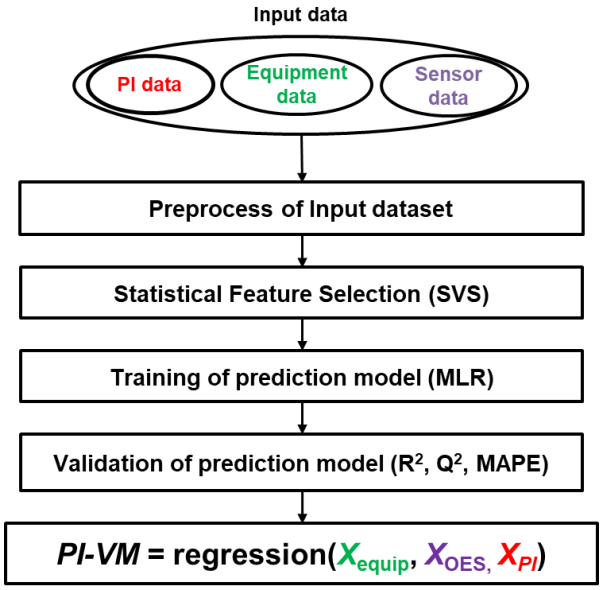

Figure 4.2 Sequence to develop PI-VM proposed by Jang et al. [11]

As referred in chapter 1, in semiconductor manufacturing, monitoring of important process variables is hard because the process is done inside vacuum reactor. Therefore, prediction of process results with statistical method, known as virtual metrology (VM), has been developed and used to monitor the process results. In the perspective of process monitoring, VM could be efficient, however, to decide control knobs and develop controllers, the plasma information based VM (PI-VM) is essential as PI-VM selects features among plasma information variables which have strong and direct relation to

process results.

Figure 4.2 is the flowchart to develop phenomenology-based and statistically-tuned PI-VM proposed by Jang et al. [11] The target variable was selected as the etch depth after the PM in section 2.3. To get input data set, the photoresist patterned Si wafer coupons were etched after the chamber wall cleaning with ethanol. Repeating 35 etches, equipment data, sensor data and PI variables were gathered and the etch depth data were measured from the normal section SEM images of the etched coupons. The etch depth was defined as the vertical distance from the bottom layer of the photoresist mask to the bottom layer of the etched Si trench as described in section 2.3. The EES data consisted of forwarding power, reflected power, capacitor positions of the matchers, operating pressure, throttle valve position and gas flow rates. The OES sensor data were composed of 4096 intensities of the CCD pixels which have wavelength from 240 nm to 1025 nm. PI variables were obtained from OES sensor data following to methods mentioned in 2.2.

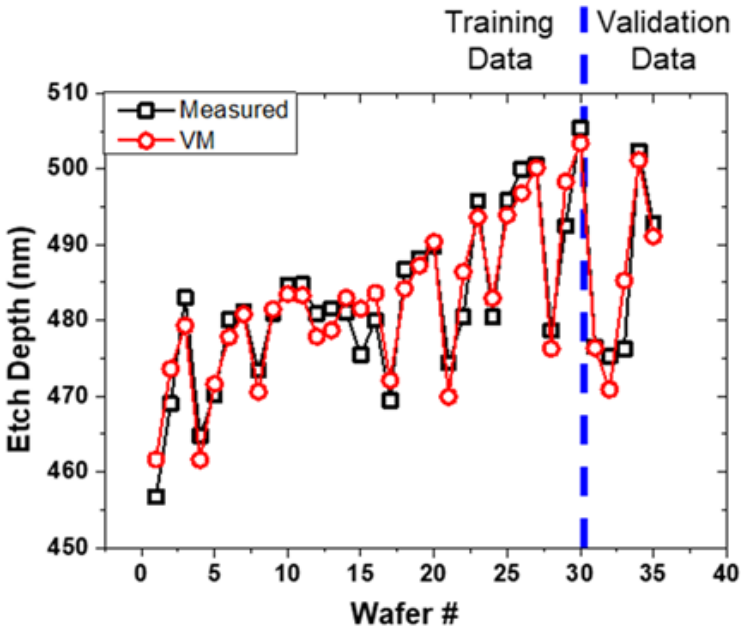

Figure 4.3 Measured etch depth by SEM analysis and predicted etch depth with PI-VM model.

$$\mathrm{ED}_{\text{PI-VM}} = \sum_i w_i X_i = w_{n_F} n_F + w_{n_H} n_H + w_{T_e} T_e + w_{TVP} TVP + w_{C_{load}} C_{load} \quad (26)$$

The PI-VM model was trained with randomly selected 30 data sets by using the multiple liner regression method based on the stepwise variable selection method provided by IBM SPSS Statistics 25 while the other data sets were used as validation data. Equation (26) is the trained PI-VM model which expressed the process results as weighted linear summation of features. The PI-VM results and the performance of the PI-VM model are drawn in Figure 4.3 and 4.4. The performance of the PI-VM model was evaluated using R^2, Q^2 and mean absolute percentage error (MAPE) following to Roh et al. [10] The

R^2 represents the goodness of fit of training records

$$R^2 = 1 - \frac{\sum_{i=Training} (y_i - \hat{y})^2}{\sum_{i=Training} (y_i - \bar{y})^2} \tag{27}$$

The Q^2 represents the R^2 for the validation records,

$$Q^2 = 1 - \frac{\sum_{i=Validation} (y_i - \hat{y})^2}{\sum_{i=Validation} (y_i - \bar{y})^2} \tag{28}$$

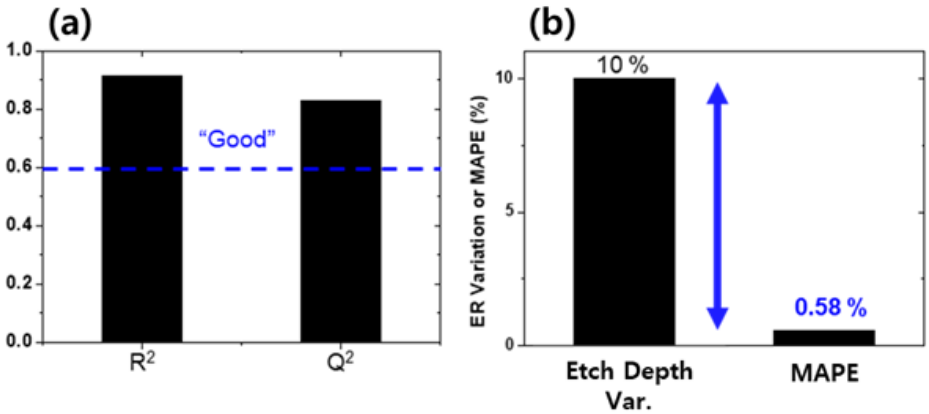

Figure 4.4 (a) R^2 and Q^2 of the PI-VM model to check goodness of fit. (b) etch depth variation by first wafer effect and MAPE of PI-VM.

The general requirements for a sound VM model are as follows; the values of both R^2 and Q^2 should be high (at least 0.5) and the difference between R^2 and Q^2 should not be too large. If the difference is too large, VM model is over-fitted. The R^2 of the PI-VM model was 0.914 and the Q^2 of the PI-VM model was 0.83 which means that the model predicts the etch depth after the wall cleaning well without overfitting.

The MAPE of the VM model could be obtained by

$$MAPE = \frac{\sum_i \left| \left(y_i - \hat{y}_i \right) / y_i \right|}{N} \times 100 \left(\% \right) \tag{29}$$

The MAPE should be smaller than the variation of the measured value to recognize the desired variation. The MAPE of the PI-VM model was 0.58 % which was much smaller than the wafer-to-wafer etch depth variation after the wall cleaning, 12 %. Therefore, the PI-VM model is proper to monitor the variation of the etch depth after the wall cleaning.

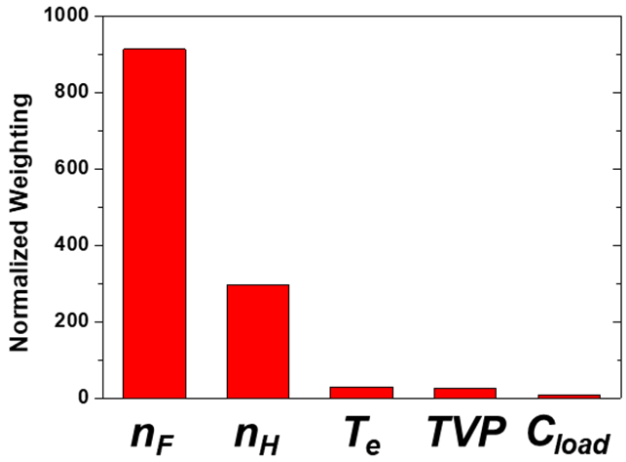

Figure 4.5 Features and normalized weightings of the PI-VM

The features of the PI-VM model and the normalized weightings of them were shown in Figure 4.5. The magnitude of normalized weightings indicates the importance of the variable in determination of etch depth. The normalized weighting of the fluorine atom density was the highest and positive which means the PI-VM model implies that the chemical surface reaction between Si and F dominates etch rate in our system. The normalized weighting of the hydrogen atom density was the second highest and negative which describes the hydrogen atom desorbed from the wet cleaned wall easily reacts with

fluorine to form HF which results in decrease of etch rate. The density of hydrogen atoms decreased as the etch process is repeated after the wall cleaning while the density of fluorine atoms increased. Therefore, the root cause of the first wafer effect in our system was due to the loss of fluorine atoms in etching plasma by recombination reaction with hydrogen atoms desorbed from the ethanol cleaned wall.

To resolve the first wafer effect, compensating the loss of fluorine in initial wafers is needed. As normalized weighting of the fluorine density is the highest and the density of hydrogen atoms is not controllable as it represents disturbance by the change of the wall condition, the fluorine density was selected as the control knob.

4.2 Develop inner loop controller

4.2.1 Selection of Manipulated Variable (MV)

The inner loop controller received set points of PI from the outer controller and adjusted the equipment recipe to follow the set points of PI. As the controlled variable (CV) of the inner controller was chosen as the density of fluorine atoms in section 4.1, manipulated variable (MV) of the inner controller should be selected. The balance equation for fluorine density in $SF_6/O_2/Ar$ etch plasma is described as below.

$$\frac{dn_F}{dt} = n_e n_{SF_6} K_{e-diss.} V + n_O n_{SF_X} K_{m-diss.} V - n_F K_{etch} A_{etch} - n_F K_{wall} A_{wall} - n_F S_{eff,F} \quad (30)$$

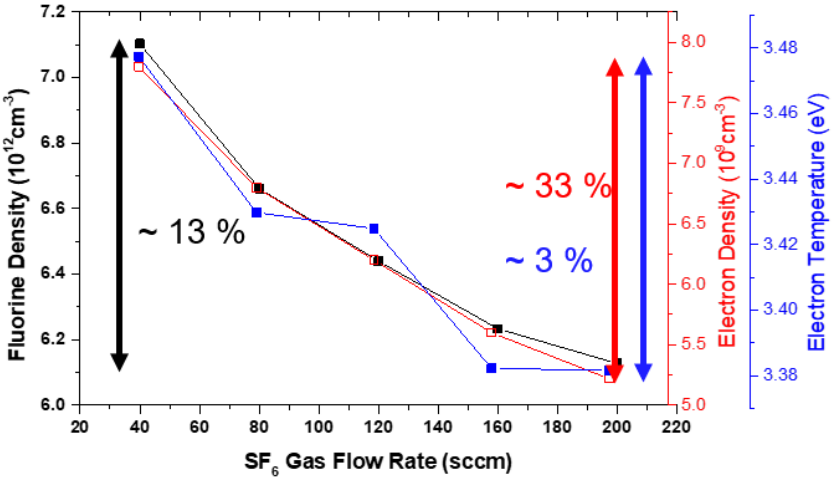

Figure 4.6 Variation of fluorine density, electron density and electron temperature with SF_6 gas flow rate variation.

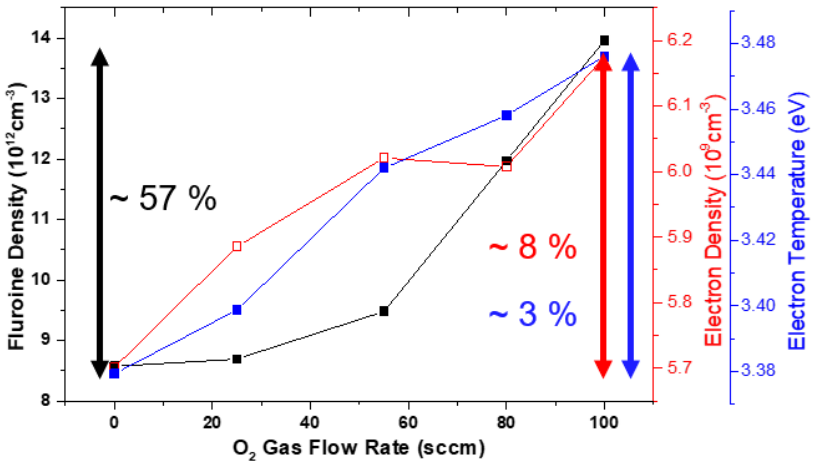

Figure 4.7 Variation of fluorine density, electron density and electron temperature with O_2 gas flow rate variation.

The first term of right-hand side represents electron impact dissociation of SF_6, the second term is dissociation of SF_x due to collision with O radical, the third term is surface loss of fluorine atoms at the etching target, the fourth

term is surface loss of fluorine atoms at the wall and the fifth term is pumping out of fluorine atoms. Fluorine atoms are mainly generated from two reaction paths: electron impact dissociation of SF_6 and mutual collision reactions between SF_x and O radical. Therefore, gas flow rates of both SF_6 and O_2 could be candidates for MV. However, as SF_6 captures electrons much more easily than O_2, manipulating SF_6 gas flow rate disturbed electron density as much as controlling the density of fluorine atoms while the variation of O_2 gas flow has much weaker effects on electron density (8 %) and temperature (3 %) than fluorine density (65 %), following to Figure 4.7 and 4.8. As good MV should have minimum perturbation on other parameters [23], O_2 gas flow rate from MFC was selected as the MV of the controller.

4.2.2 Dynamic Modeling based on Particle Balance Equation

As referred in section 3.1, the Equipment – PI controller is based on dynamic equilibrium of the plasma which could be described by phenomenological model. The dynamic model describing the reaction of fluorine atom density following to change of O_2 gas flow rate could be gotten by rearrangement of the particle balance equation (30). The variation of O_2 gas flow would change the fluorine atom density by mutual reaction of O and SF_x written as the second term of the equation (30) Therefore, the oxygen atom density balance equation should be described.

$$\frac{dn_O}{dt} = n_e n_{O_2} K_{e-diss.} V - n_O n_{SF_x} K_{m-diss.} V - n_O S_{eff,O} \tag{31}$$

The oxygen atom in $SF_6/O_2/Ar$ etch plasma generated by electron impact

dissociation of O_2 molecule and lost by collisions with SF_x molecules and pumping out. The balance equation for O_2 molecule density could be written as below.

$$\frac{dn_{O_2}}{dt} = Q_{O_2,Showerhead} - n_e n_{O_2} K_{e-diss.} V - n_{O_2} S_{eff,O_2} \tag{32}$$

O_2 molecules in $SF_6/O_2/Ar$ plasma are supplied by MFC through the showerhead, $Q_{O2,showerhead}$, and lost by electron impact dissociation reactions and pumping out. Therefore, O_2 molecule density could be written as below.

$$n_{O_2} = \frac{Q_{O_2,Showerhead}}{S_{eff,O_2} + n_e K_{e-diss.} V} - e^{\left(n_e K_{e-diss.} V + S_{eff,O_2}\right)t} \tag{33}$$

As the chemical reactions like dissociation and surface loss reactions are almost 105 times faster than mechanical reactions by actuators like gas delivery time through gas pipes and the showerhead, and throttle valve settling time, chemical reactions could be treated as instant reactions and the time characteristics of actuators dominated the dynamics. Including the delay time from MFC to showerhead through gas pipes, the Laplace transformed $\Delta Q_{O2,showerhead}$ could be written as below

$$\Delta Q_{O_2,Showerhead} = \frac{\Delta Q_{O_2,MFC}}{\tau_{MFC} s + 1} e^{-\tau_{d,MFC} s} \tag{34}$$

where $\Delta Q_{O2,MFC}$ is the variation of gas flow at the output of MFC, τ is the rise time of the MFC, and $\tau_{d,MFC}$ is the delay time. Therefore, the Laplace transformed relation between O_2 gas flow rate from MFC and fluorine atom density could be described by rearrangement of equation (30~34).

$$\Delta n_F = \frac{G}{\tau_{MFC} s + 1} e^{-\tau_{d,MFC} s} \Delta Q_{O_2} \left(G = \frac{n_e n_{SF_6} K_{e-diss.} V + n_O n_{SF_X} K_{m-diss.} V}{K_{etch} A_{etch} + K_{wall} A_{wall} + S_{eff,F}} \right) \quad (35)$$

In equation (35), G is the gain of the control model which represents the balance between generation of fluorine atom by electron impact dissociation of $SF_6$and mutual reaction of O radical and loss of fluorine atom by Si etching, wall loss and pumping out. As O_2 gas flow rate varies, electron density, partial pressure of SF_6 gas, O radical density and SF_x density are also changed and the gain of the control model is not constant which means nonlinear relation between O_2 gas flow rate and fluorine atom density. The calculation of the gain requires solving full particle balance equations for the $SF_6/O_2/Ar$ etching plasma, however, it is impossible to measure absolute densities of every species in the plasma and get proper cross-section data for some reactions. Thus, to get the gain, cross-section data for major reactions obtained by Christophorou [25] and Ryan [26] was used, PI variables like electron density, electron temperature, radical density were measured as input data, surface loss reaction was modeled from etch rate of bare Si coupons and the density of SF_x was assumed to be in proportion with fluorine atom density as they both generated from SF_6.

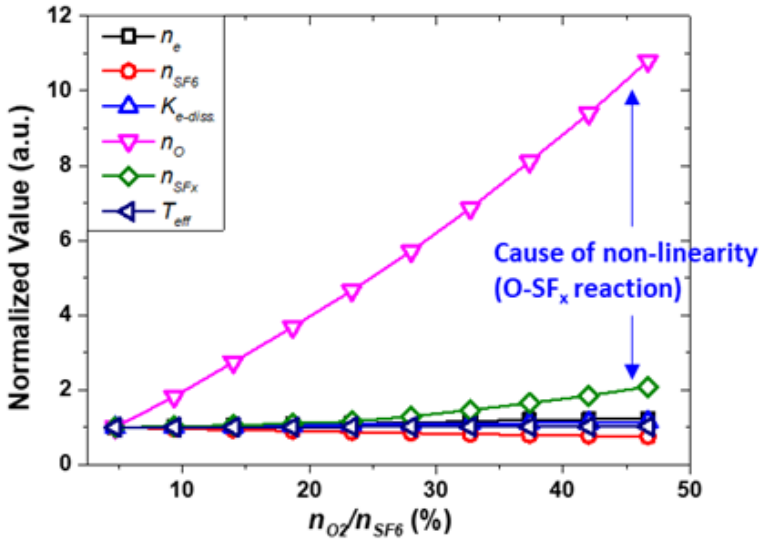

Figure 4.8 Variation of parameters in fluorine atom balance equation with variation of O_2 gas mixing ratio to SF_6 gas.

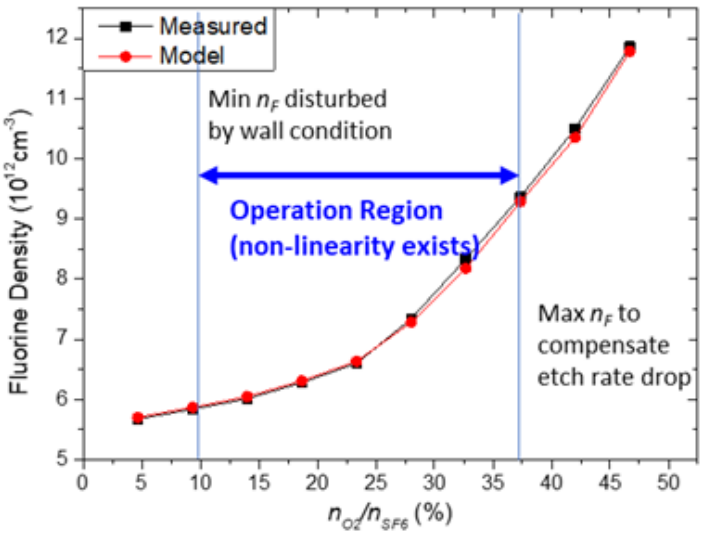

Figure 4.9 Variation fluorine atom density with variation of O_2 gas mixing ratio to SF_6 gas.

Figure 4.8 is the variation of the parameters composing the gain following to the variation of O_2 gas flow rate. The nonlinearity between fluorine atom density and O_2 gas flow rate was mainly due to the increase of O radical density and SF_x density as O_2 gas flow rate increases which agrees with the experiments by Ryan et al. [26]. Figure 4.9 is the fluorine atom density measured by actinometry described in section 2.2.3 and calculated from the particle balance equation. The model could describe nonlinear relation between fluorine atom density and O_2 gas flow rate well and for the sequential etch processes referred in section 4.1, the minimum fluorine atom density disturbed by wet cleaning of the wall by ethanol and the maximum fluorine atom density required to compensate the first wafer effect in initial wafer covers the nonlinear relation. Therefore, in the operation region of this thesis, nonlinear control algorithm is needed.

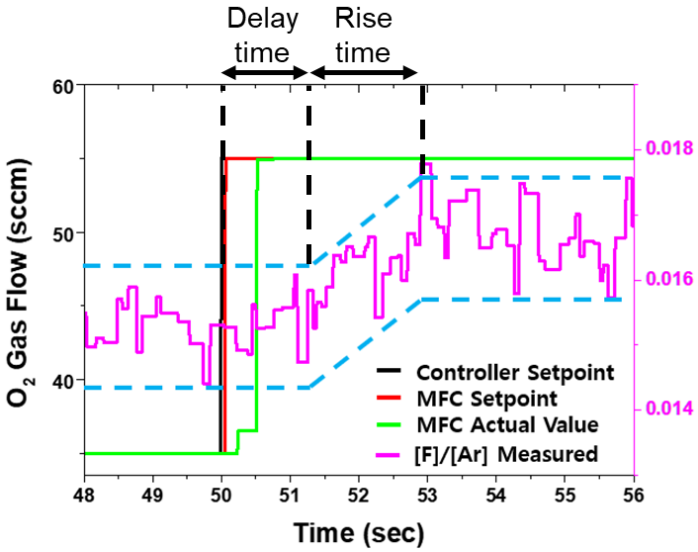

Figure 4.10 Step change fluorine atom density with step change of O_2 gas flow rate.

The time constant and dead time of the controller represented the gas delivery time from the MFC to the showerhead through the gas lines and the settling time of throttle valve to keep the pressure constant. The gas delivery time was measured as 750 msec and the settling time of the throttle valve was measured as 1.65 sec by monitoring variation of atomic fluorine density after the gas injection shown in Figure 4.10.

4.2.3 Multiple Gain Model Predictive Controller

As mentioned in previous section, control of fluorine atom density by O_2 gas flow rate requires nonlinear control algorithm. There are two methods for nonlinear MPC; ordinary differential equation (ODE) based controller and multiple gain MPC. The ODE based controller solves the particle balance equation (30) iteratively and calculates control moves. However, in this thesis, the particle balance equation is not self-consistent model and uses PI variables measured by OES. Therefore the noise in PI variables could make the calculation unstable. In multiple gain MPC, the gains for separated operation regions are pre-calculated and the controller uses each gains for each regions. Thus, in this thesis, multiple gain MPC was chosen to develop nonlinear controller for O_2 gas flow rate – fluorine atom density.

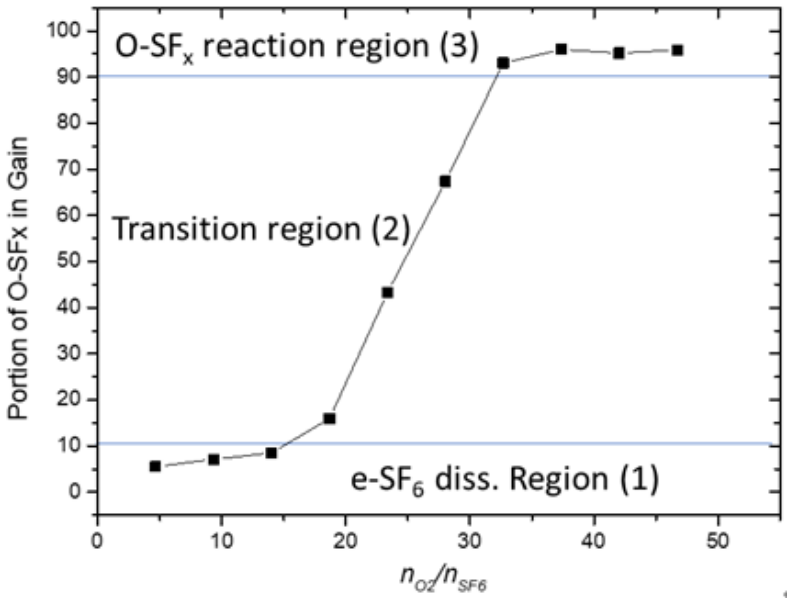

Figure 4.11 Portion of O-SFx mutual reaction in total fluorine atom generation gain with O2 gas variation.

$$G = \frac{n_F\,'}{\Gamma_{O_2}\,'} = \frac{\left(n_e n_{SF_6} K_{e-diss.}\left(T_{eff.}\right)V\right)'}{\Gamma_{O_2}\,'} + \frac{\left(n_O n_{SF_X} K_{m-diss.} V\right)'}{\Gamma_{O_2}\,'} \tag{36}$$

The gain in equation (35) could be rewritten as equation (36), the first term of the right-hand side means the portion of electron impact SF_6 dissociation for the gain and the second term of the right hand side means the portion of mutual reaction by O radical and SF_x for the gain. Figure 4.11 represents the portion of O-SF_x mutual reaction in the gain following to O_2 molar ratio. For O_2 molar ratio under 15 %, electron impact dissociation of SF6 dominates the gain while for O_2 molar ratio over 30 %, O-SF_x mutual reaction dominates the gain. Therefore, the nonlinear gain could be divided into three linear gain regions following to the dominant fluorine generation reaction. The gains for

each region were calculated by the model and tested by set-point tracking test.

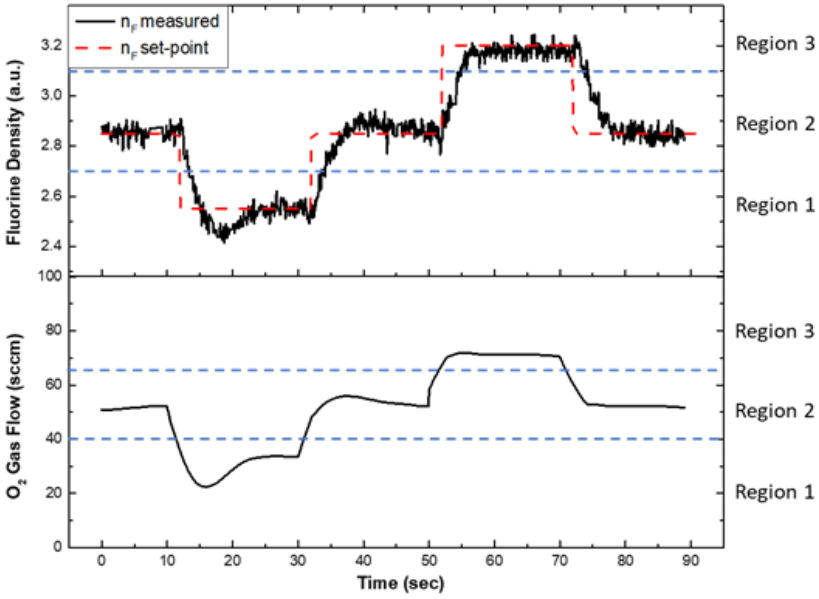

Figure 4.12 Set-point tracking test of GSMPC for region 1,2, and 3.

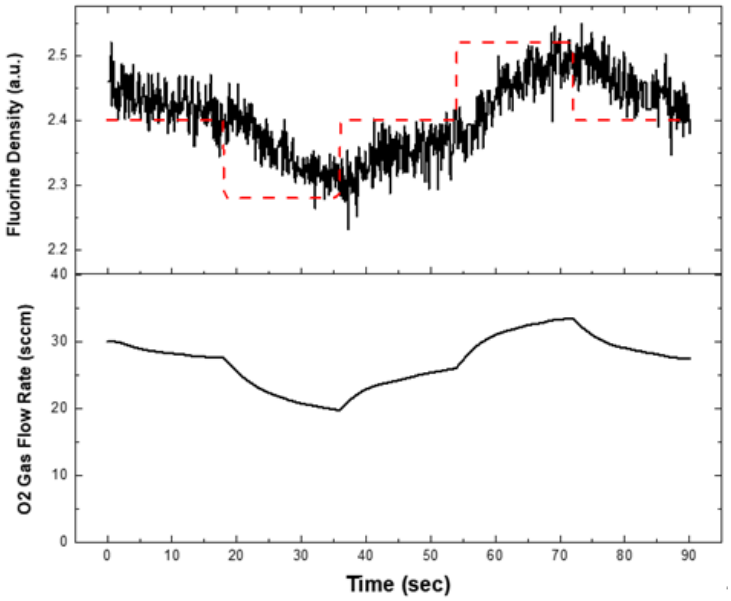

Figure 4.13 Set-point tracking test of MPC for region 3 at region 1.

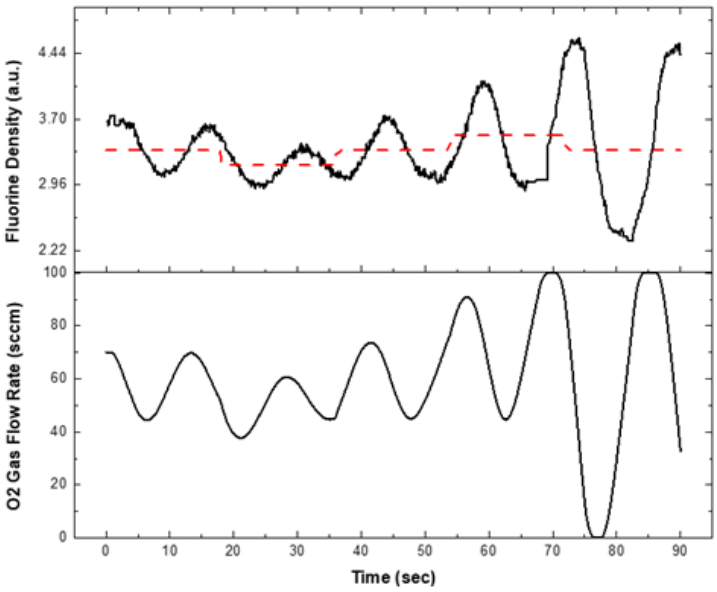

Figure 4.14 Set-point tracking test of MPC for region 1 at region 3.

To confirm the performance of the inner loop controller, set-point tracking test was done for disturbance free condition. Figure 4.12 is the set-point tracking test with multiple gain MPC for three regions, figure 4.13 is the set-point tracking test with region 3 MPC applied to region 1, figure 4.14 is the set-point tracking test with region 1 MPC applied to region 3. For mismatched control gain and operation region, higher gain than operating region results in under estimation of control action shown in figure 4.13 and lower gain than operating region results in over estimation of control action shown in figure 4.14. For the multiple gain MPC, the controller automatically changes gain for operating region showing better performance than the other two cases. The multiple gain MPC could handle 15 % variation of atomic fluorine density within 3 sec and keep the integrated error under 1 % which means the

performance of the inner loop controller is enough to compensate the first wafer effect under 1 % error.

4.3 Develop outer loop controller

4.3.1 Linearization of Control Model

The outer controller received process results from PI-VM and calculated required PI to satisfy the desired the process results in time. In this case, the desired etch depth was 480 nm and the desired etch time was 1 minute. In section 4.1, PI-VM model to monitor etch depth was developed and the manipulated variable of outer loop was selected as fluorine atom density.

$$\mathrm{ED}_{\text{PI-VM,k}} = \sum_{i=1}^{k}\left(w_{PI_F} PI_{F,i} + w_{PI_{wall}} PI_{wall,i} + w_{PI_{T_e}} PI_{T_{e,i}} + w_{TVP} TVP_i + w_{C_{load}} C_{load,i} \right) \quad (37)$$

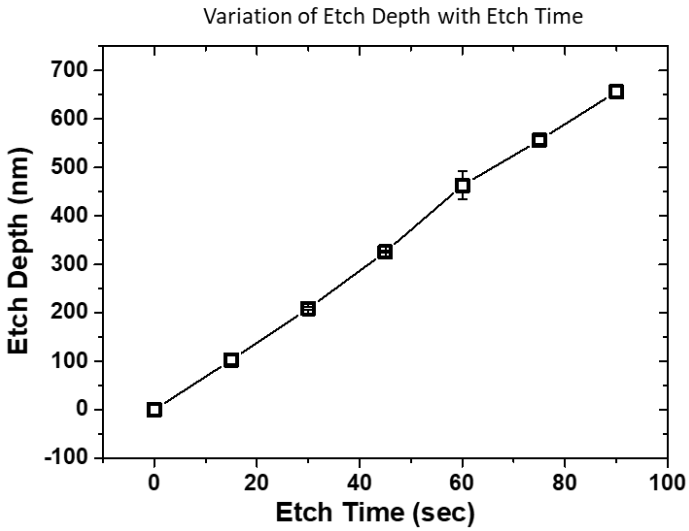

Figure 4.15 Etch Depth variation measured by SEM image analysis with various etch times for reference etch recipe.

The features of the PI-VM, such as fluorine atom density, wall condition, electron temperature, throttle valve position and load cap position, are in dynamic equilibrium while the process is going on. However, the process results, predicted by PI-VM, is time integrated result of surface reaction. Therefore, to develop real-time controller with PI-VM, dividing etch depth as etch rate for each moment should be ensured. Figure 4.15 shows that the etch depth measured from cross-section SEM image analysis corresponds with the time divided PI-VM which means it is available to describe etch depth as summation of etch rate predicted with features in dynamic equilibrium.

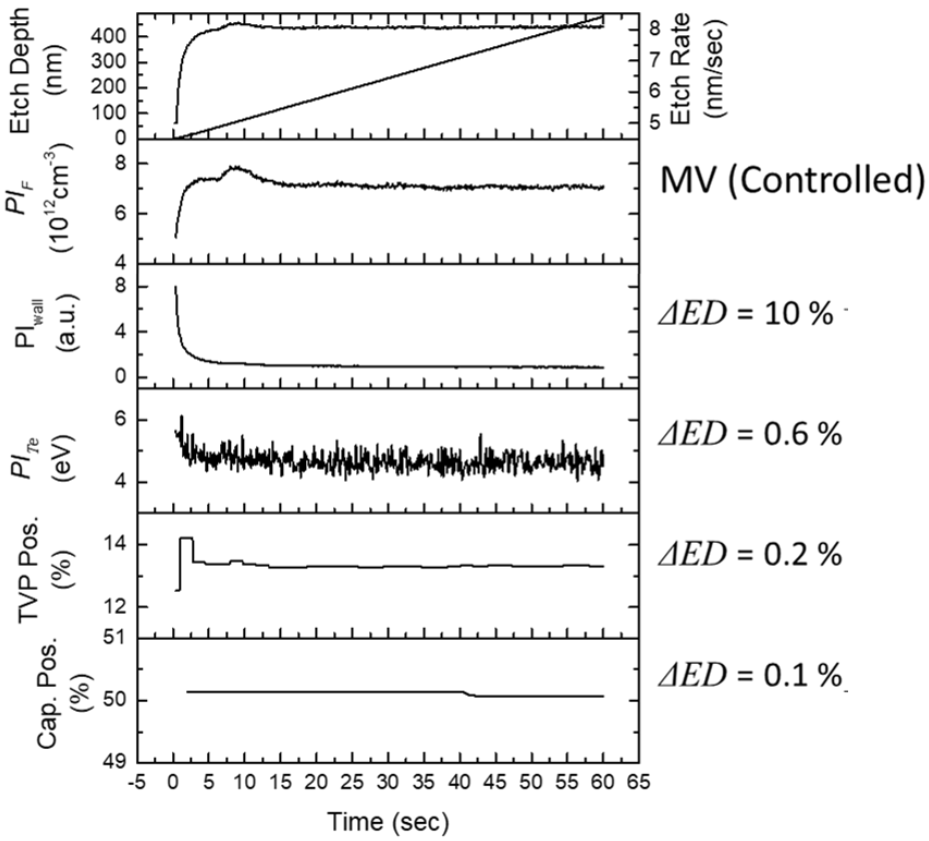

Figure 4.16 Time transition of features of PI-VM while etch process is running.

As described in equation (37), the etch depth is not determined by only the manipulated variable; fluorine atom density. The effect of other features like wall condition, electron temperature, throttle valve position and load cap position should be evaluated to linearize the outer loop control model. Figure 4.16 shows the effect of other features while the process is going on. The effect was calculated by integration of weighted features divided by final etch depth. As shown in figure 4.16, the effect of wall condition is 10 %, which is

not negligible while the effects of the other features were under 1 %.

$$\frac{dn_H}{dt} = -n_H K_{wall} A_{wall} \tag{38}$$

$$n_H = y_0 + A_1 \exp\left(-x / t_1\right) \tag{39}$$

$$\int_{t_k}^{t_{end}} n_H = y_0 \left(t_{end} - t_k\right) + A_1 t_1 \left(e^{-t_k / t_1} - e^{-t_{end} / t_1}\right) \tag{40}$$

To remove the effect of wall condition in control model, prediction of variation of wall condition during the process should be modeled. The wall condition was estimated by hydrogen density in the etch plasma, as the hydrogen residue acts as sink of fluorine density by recombination reaction, equation (38). The residual hydrogen on the wall has no source but sink. Therefore, the hydrogen density could be described by exponential decay model, equation (39). The effect of wall condition during the process could be calculated by integration of exponential variation of hydrogen density from current time step to the final time step as equation (40). Rearrange the equation (37) with equation (40) and neglect effect of disturbances other than wall condition brings the linear relation between etch depth and fluorine atom density as below.

$$PI_{F,k+1} - PI_{F,k} = \begin{pmatrix} \dfrac{ED_{set} - ED_k}{t_{set} - t_k} - \int_k^n w_{PI_{wall}} PI_{wall,k} dt \\ -\left(t_n - t_k\right)\left(w_{PI_{T_e}} PI_{T_e,k} + w_{TVP} TVP_k + w_{C_{load}} C_{load,k}\right) \end{pmatrix} / w_{nF} \tag{41}$$

4.3.2 Shrink Horizon Model Predictive Controller

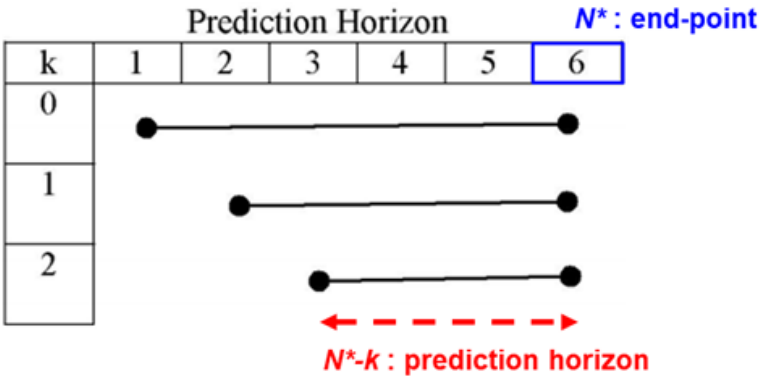

Figure 4.17 Schematic of shrink horizon model predictive controller

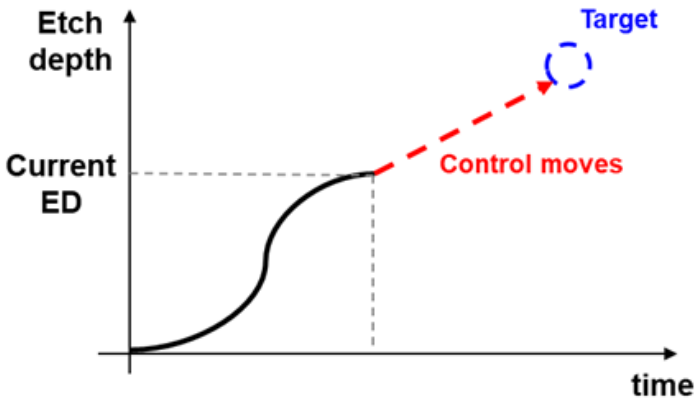

Figure 4.18 Outer loop control algorithm to achieve target etch depth in target etch time based on current etch depth and current time

As mentioned in section 4.4.1, the set point of outer loop is time integration of surface reaction described by PI-VM model composed of features in dynamic equilibrium. Therefore, the control algorithm should consider the control moves from the current step to the final step of the process unlike the

controllers developed in section 3.1 and 4.2, receding horizon controllers. For process results in semiconductor manufacturing, shrink horizon model predictive controller (SHMPC) could be used to control final process results with dynamic equilibrium states for each moment. The SHMPC predicts variation of controlled variable from the current time step to the end point and calculates best control move of manipulated variable as shown in figure 4.17. In this thesis, the etch depth of current moment was calculated as summation of PI-VM of previous time steps and the control moves were calculated to keep constant etch rate for the remaining process time to satisfy the target etch depth and the target time. As the relation between etch depth and fluorine atom density was linearized in previous section, the control moves are presented as set points of fluorine atom density for next time steps as below.

$$PI_{F,k+1} - PI_{F,k} = \begin{pmatrix} \dfrac{ED_{set} - ED_k}{t_{set} - t_k} - \int_k^n w_{PI_{wall}} PI_{wall,k} dt \\ -\left(t_n - t_k\right)\left(w_{PI_{T_e}} PI_{T_e,k} + w_{TVP} TVP_k + w_{C_{load}} C_{load,k}\right) \end{pmatrix} / w_{nF} \qquad (42)$$

Following to D. E. Seborg et al., the inner loop should be 5~10 times faster than the outer loop, as rule of thumb. [23] Therefore, the outer loop controller calculated and sent the required fluorine atom density every 0.5 seconds while the inner loop controller developed in section 4.3 adjusted O_2 gas flow rate every 0.1 seconds.

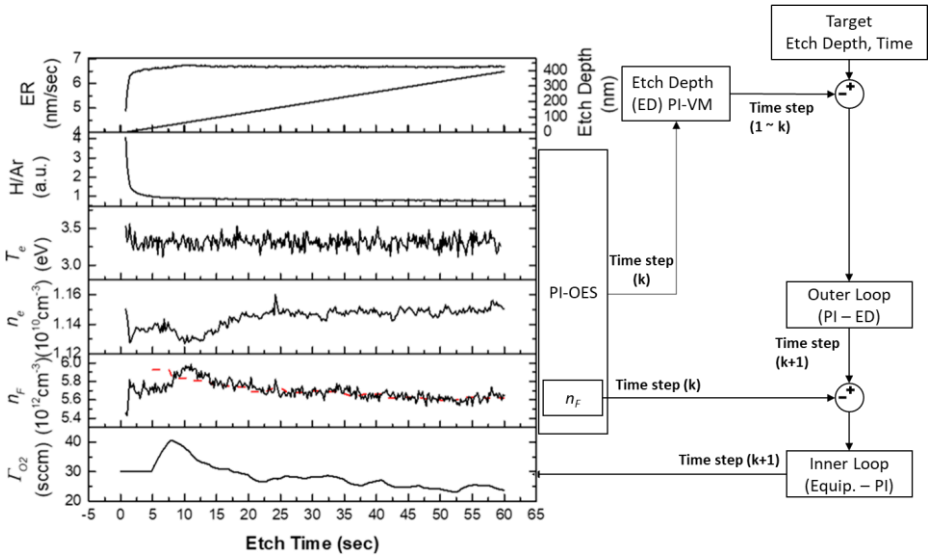

Figure 4.19 Schematic of 2 loop controller and actual real-time data in control system.

Figure 4.19 is the schematic of 2 loop controller, connection of inner loop controller and outer loop controller. From the real-time sensor data, etch depth of current time was calculated with the PI-VM model and the outer controller received it to calculate required fluorine atom density to compensate the first wafer effect. The outer loop controller delivers set point of fluorine atom density for 5 steps of the inner loop controller and the inner loop controller adjusted O_2 gas flow rate to satisfy the set point of fluorine atom density. This process is repeated until the target time and target etch depth is achieved.

4.3.3 Operation window of PI-APC

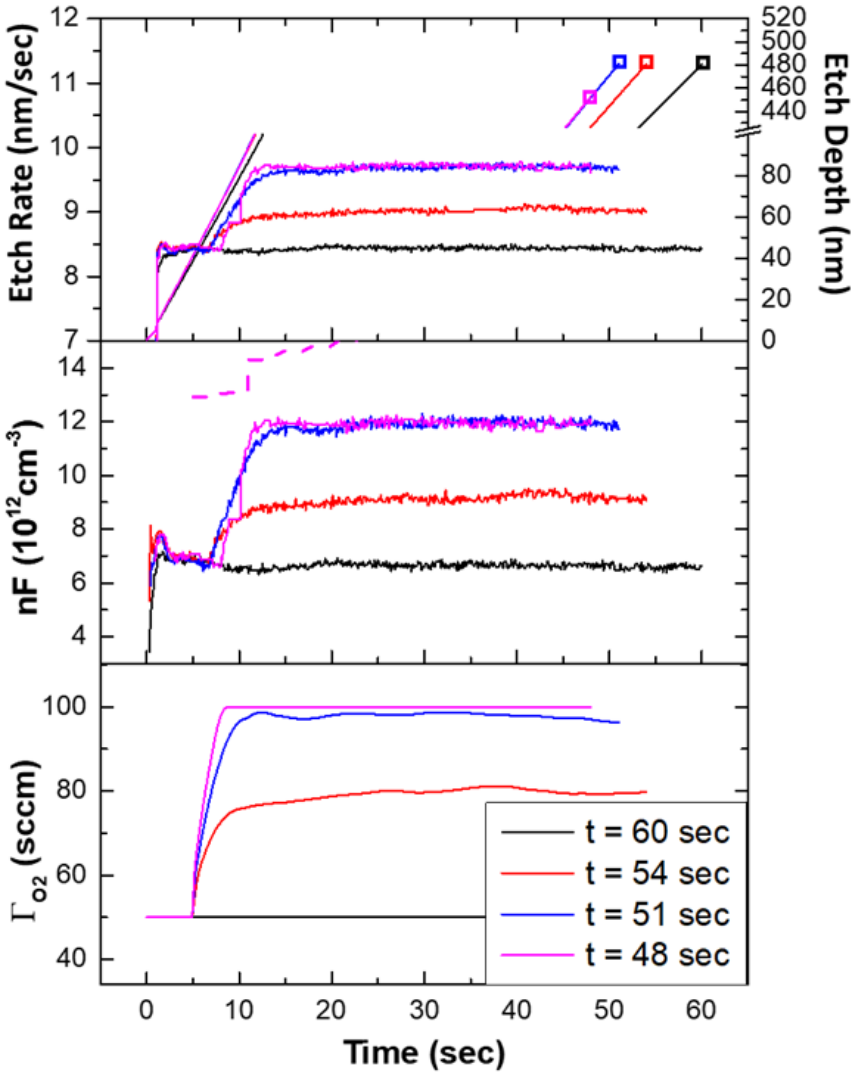

Figure 4.20 Reduce etch time test for 60, 54, 51 and 48 seconds with same etch depth goal.

To confirm the performance of the PI-APC, adjusting etch time for same etch depth was tested in disturbance free condition. The set point of etch depth

was 480 nm as same as the nominal condition but the set point of etch time was reduced from 60 sec to 54, 51 and 48 sec. To satisfy the etch depth in shorter etch time, the outer loop controller increased etch rate which delivered to the inner loop controller as the set point of fluorine atom density. To satisfy faster etch rate, the inner loop controller increases O_2 gas flow rate to enhance the generation of fluorine atom density by O-SF_x mutual reaction. Therefore, for shorter etch time, higher fluorine atom density and higher O_2 gas flow rate could be found in figure 4.20. However, as the MFC of O_2 gas has maximum flow rate limitation at 100 sccm, the inner loop controller could not increase fluorine atom density to the set point in 48 sec etch time process, where the set point of fluorine atom density is drawn as dotted magenta line. Therefore, for the PI-APC developed in previous section, the limitation of fast etch process is determined by hardware specification of O_2 MFC and the etch time could be reduced to 51 sec (15 %).

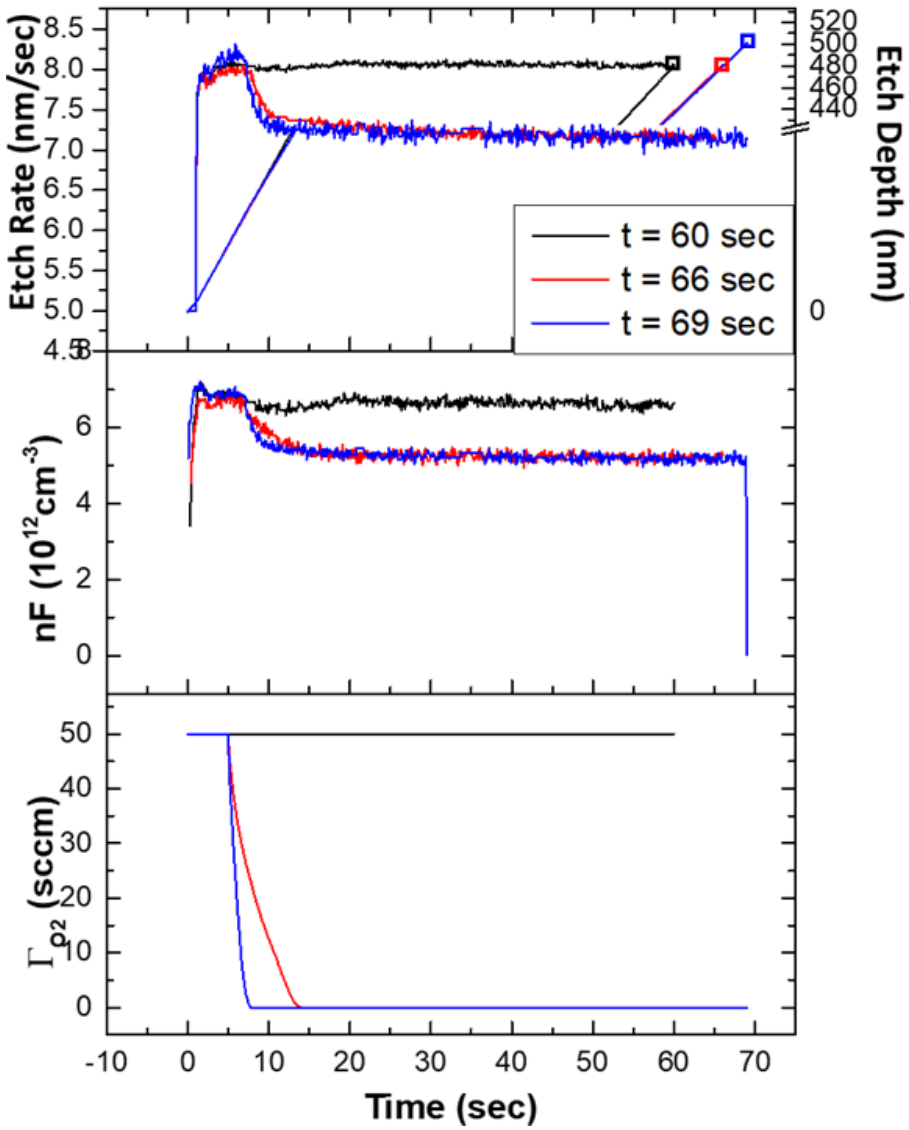

Figure 4.21 Increase etch time test for 60, 66 and 69 seconds with same etch depth goal.

For longer etch time cases, the set point of etch depth was also fixed at 480 but the set point of etch time was increased from 60 sec to 66 and 69 sec. To satisfy the etch depth in longer etch time, the outer loop controller decreased etch rate which delivered to the inner loop controller as the set point of fluorine atom density. To satisfy slower etch rate, the inner loop controller decreases O_2 gas flow rate to decrease the generation of fluorine atom density by O-SF_x mutual reaction. Therefore, for longer etch time, lower fluorine atom density and lower O_2 gas flow rate could be found in Figure 4.21. Identical to the faster etch cases, the inner loop controller could not decrease fluorine atom density to the set point in 69 sec etch time process as the MFC of O_2 gas has minimum flow rate limitation at 0 sccm. Therefore, for the PI-APC developed in previous section, the limitation of slow etch process is determined by hardware specification of O_2 MFC and the etch time could be increased to 66 sec (10 %). The difference in the limitation range for faster and slower etch process is came from the nonlinearity of the relation between fluorine atom density and O_2 gas flowrate which was covered in section 4.2.2.

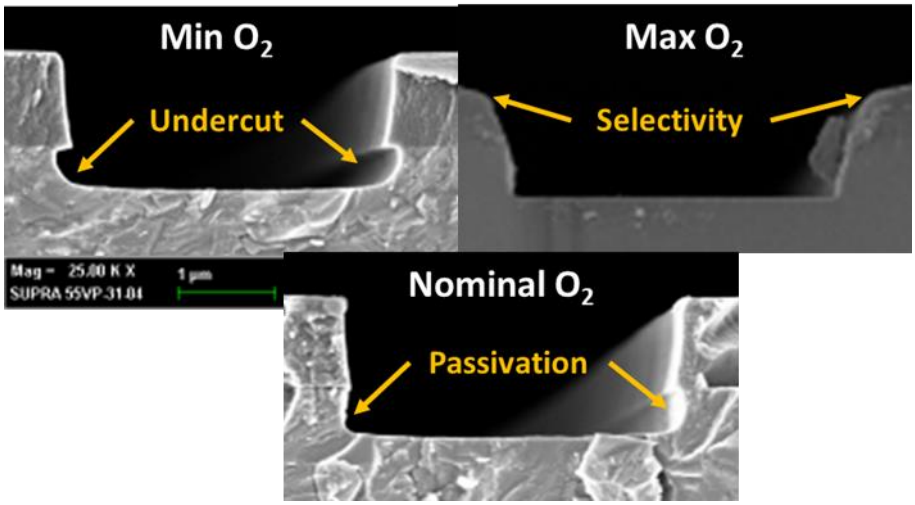

Figure 4.22 Portion of O-SFx mutual reaction in total fluorine atom generation gain with O2 gas variation.

Furthermore, the increase and decrease of O_2 gas flow rate to maximum and minimum results in change of process results other than etch depth as shown in figure 4.22, the limitation of SISO-SISO controller. For minimum O_2 case, passivation layer, SiO_xF_y, could not be formed at the side wall and results in more isotropic etch, undercut. For maximum O_2 case, anisotropic etch was done due to abundant passivation layer but the O radical reacts with the PR mask and the selectivity was lower than nominal case. This limitation will be noted in future works.

4.4 Adopt PI-APC to compensate first wafer effect

Finally, the PI-APC was adopted to sequential etch processes after the ethanol cleaning of plasma facing components. As mentioned in section 2.3

the etch depth of initial two wafers were shallower than the etch depth of later two wafers and the variation of etch depth was stabilized at the third wafer. PI-APC was adopted to keep the etch depth as steady regardless of chamber wall condition and compared to the open loop case, which means no control of etch depth.

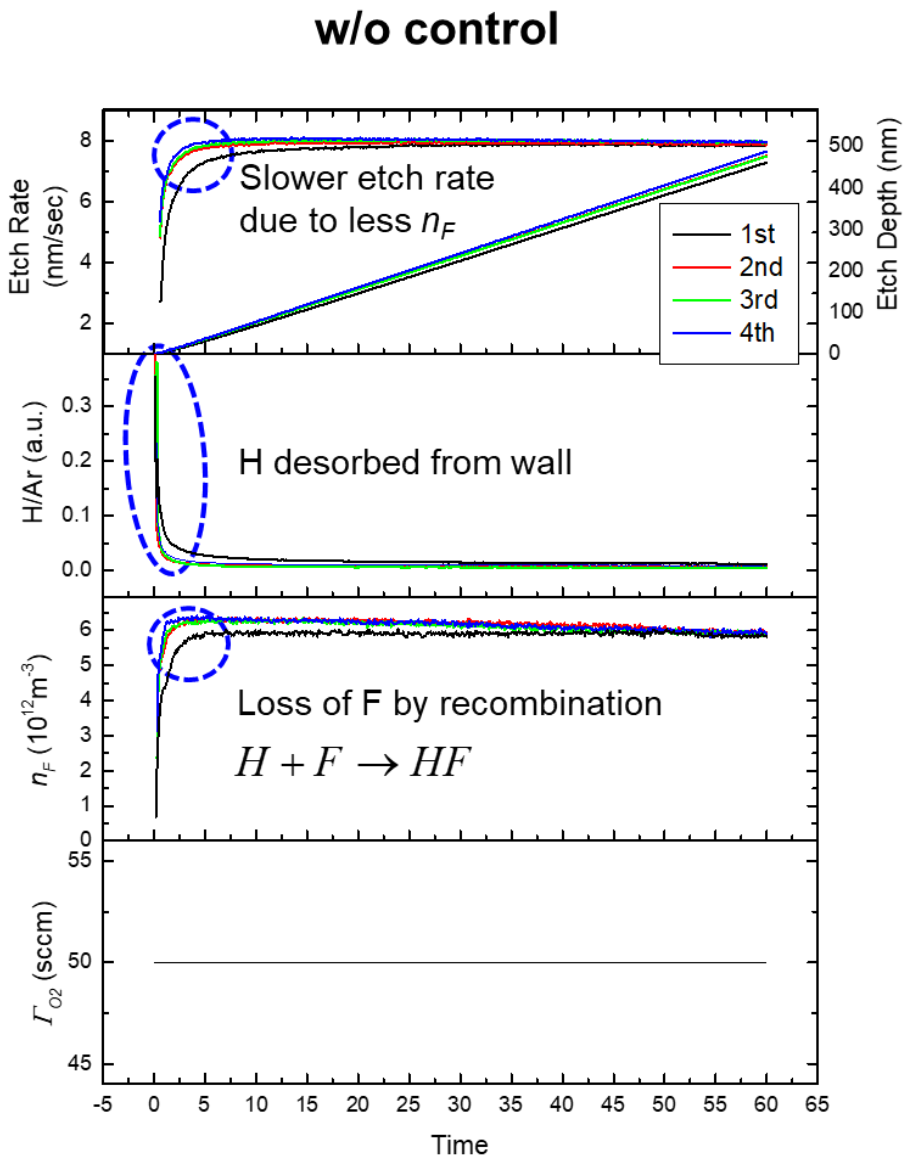

Figure 4.23 Sequential etch processes after wet cleaning of wall with fixed recipe (open loop case).

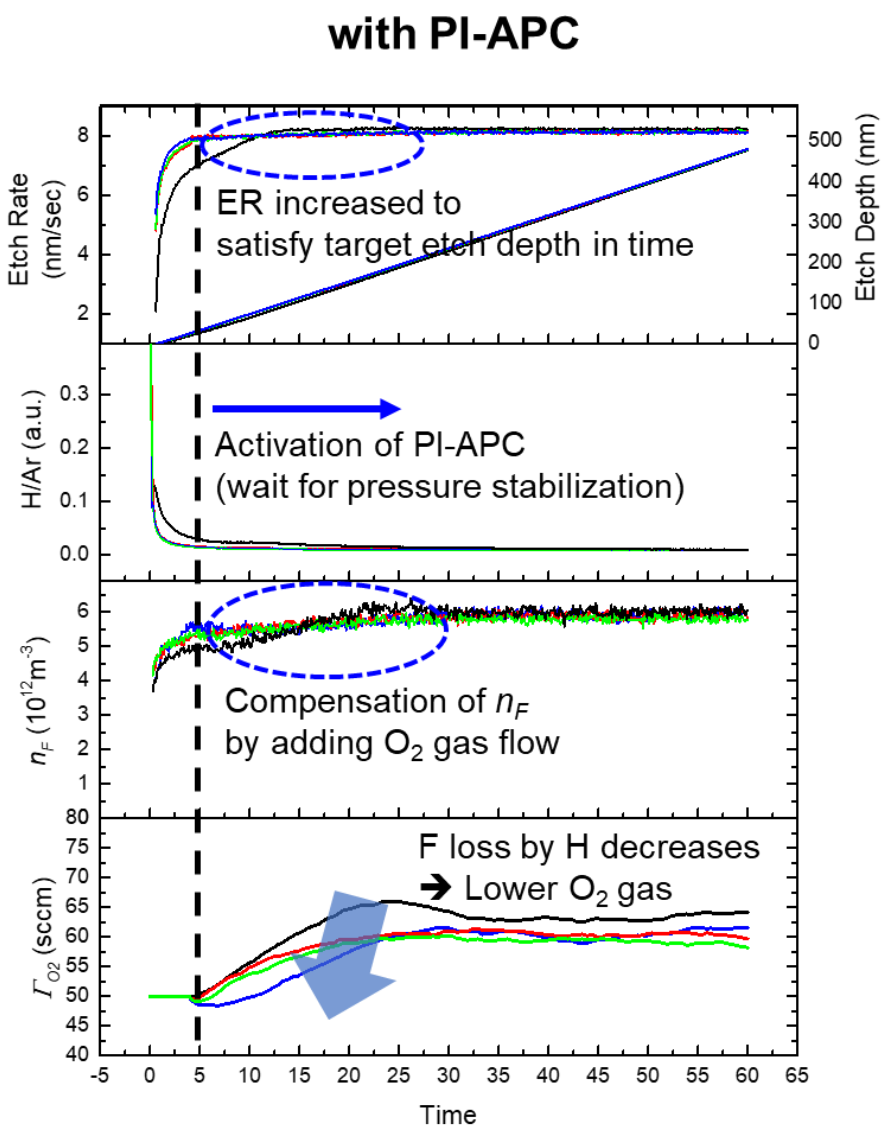

Figure 4.24 Sequential etch processes after wet cleaning of wall with PI-APC.

Figure 4.23 is the open loop case, where the recipe was fixed at nominal values, and the sequential etches after the ethanol cleaning of the wall were conducted. The etch rate of first wafer was lower than that of other wafers as

the residual hydrogen on the wall desorbed from the wall and acts as loss of fluorine atom, the etchant, by recombination reaction. As shown in figure 4.23, the hydrogen density was higher in the first wafer and lowered by repeating the etch processes. Therefore, the fluorine atom density at the first wafer was lower and increased as process time goes on (in-wafer) and the process is repeated (W2W). The root cause of the first wafer effect in this thesis was variation of residual hydrogen density on the wall and its effect on the etchant density. To compensate the first wafer effect, PI-APC compensated the decreased etch rate by increasing fluorine atom density as shown in figure 4.24. The outer loop controller recognized that the etch rate in the first wafer is lower than the nominal condition and decided to increase etch rate for the rest process time. To compensate the lower etch rate, required etchant density is calculated by the linearized algorithm described in section 4.3 and delivered to the inner loop controller developed in section 4.2. The inner loop controller increased O_2 gas flow rate to satisfy the set point of fluorine atom density while considers the nonlinearity for the operating region. As results, etch rate is compensated to reach target etch depth in target etch time and the compensation was stronger in initial wafers which is presented by higher O_2 gas flow rate in initial wafers.

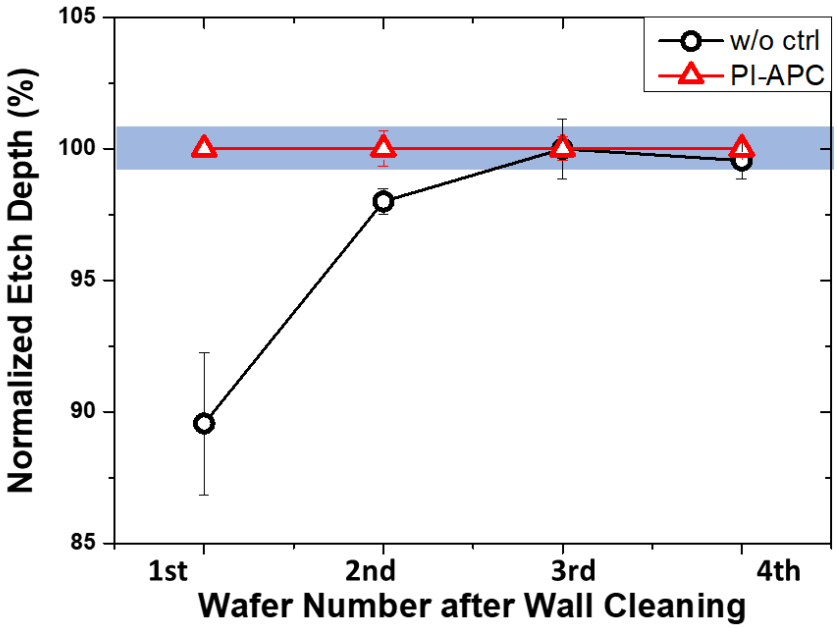

Figure 4.25 Etch depth measured by SEM image analysis for sequential etch processes after wall cleaning by ethanol. Black dots are open loop case and red dots are controlled by PI-APC

By adopting the PI-APC to the sequential etches after the wet cleaning of the wall, the variation of etch depth was decreased from 12 % to 0.5 %. The PI-APC recognize the first wafer effect by prediction on the etch depth with PI-VM model and reacts to modify the recipe by converting time integrated surface reaction into dynamic plasma property with linearized model. Regardless of the wall condition, PI-APC could achieved constant W2W etch depth by in-wafer control of etchant generation with error under 0.5 %.

Chapter 5. Conclusion

Through the division of process controller into two hierarchical control loops based on PI-VM, plasma chemistry-based SISO-SISO in-wafer controller to compensate W2W etch depth variation due to first wafer effect could be developed at the first time. The PI-VM offers information on effect of etchant and chamber wall condition to process results as features and weightings of regression model to connect time-integrated surface reaction to plasma information variable in dynamic equilibrium in form of inner loop and outer loop. The inner control loop controls generation of plasma and the outer controller loop controls time-integrated surface reactions on the process target. The inner control loop controls generation of particles based on phenomenological control model. The generation and loss balance of fluorine atoms, which acts as etchant in $SF_6/O_2/Ar$ Si etching plasma, was modeled with measured plasma information variables and chemical reaction cross-section data. From the balance equation, O_2 gas was selected as manipulated variable as it has least effects on other parameters in the balance equation while it can control fluorine atom density effectively. The nonlinear relation between O_2 and n_F was divided into three regions based on the dominant generation reaction: electron-impact dissociation, O-SFx mutual reaction, and transition region. The gain scheduled controller and phenomenological modelling enabled control of non-linear relation of O_2 gas mixing ratio to fluorine density in $SF_6/O_2/Ar$ etch plasma..

The outer control loop controls time-integrated process results based on PI-

VM model. The PI-VM showed which variables are important and how much effect they have on the process results by features and weightings. By integrating etch rates and predicting effect of time-varying wall condition by phenomenological model, the outer control loop could be linearized and calculate required fluorine density in dynamic equilibrium to achieve set etch depth at set process time.

The PI-APC showed that overcoming nonlinearity in plasma-assisted processes is available by plasma physics and chemistry model and division of controller into two hierarchical loops. The possibility to increase yield in plasma-assisted processes is shown by in-wafer controller which could handle more sophisticated problems than traditional R2R controllers. Moreover, the parameters in the controllers are expected to be used in predictive maintenance, tool-to-tool matching problems and developing optimized process recipes.

As this thesis focused on plasma chemistry control in SISO-SISO manner, further study could include interactions between plasma information variables and other process results, like anisotropy, selectivity and uniformity. From the SEM image analysis on the longest time etch and shortest time etch in section 4.3.3, even the etch depth is satisfied by the SISO-SISO controller, passivation reaction due to O_2 and ashing reaction by O_2 result in different anisotropy and selectivity. In industrial application, these process results are also significant to chip performance. Therefore, linking two SISO-SISO controllers or combining interactions between variables to develop MIMO-MIMO controllers could be developed to apply 2 hierarchical loops structure

in real process conditions.

Appendix

List of electron impact collision reactions included in calculation of collisional energy loss

Reaction		Threshold Energy	Reference
Elastic Collision	e+Ar → e+Ar		[19]
Excitation (Total)	e+Ar → e+Ar	11.5 ~ 15.6	[19]
Ionization	e+Ar → 2e+Ar^+	15.8	[19]
Elastic Collision	e+SF_6 → e+SF_6^-		[20]
Attachment	e+SF_6 → SF_5+F^-	1.8	[20]
Attachment	e+SF_6 → SF_4+F_2^-	1.4	[20]
Attachment	e+SF_6 → SF_2^-+4F	1	[20]
Attachment	e+SF_6 → SF_3^-+3F	7.5	[20]
cAttachment	e+SF_6 → SF_4^-+2F	3	[20]
Attachment	e+SF_6 → SF_5^-+F	0	[20]
Attachment	e+SF_6 → SF_6^-	0	[20]
Excitation (Total)	e+SF_6 → e+SF_6	0.08 ~ 0.48	[20]
Dissociation	e+SF_6 → e+SF_5+F	9.6	[20]
Dissociation	e+SF_6 → e+SF_4+2F	12.1	[20]
Dissociation	e+SF_6 → e+SF_3+3F	16	[20]
Ionization	e+SF_6 → 2e+SF_5^++F	15.7	[20]
Ionization	e+SF_6 →	18.5	[20]
Ionization	e+SF_6 →	18.8	[20]
Ionization	e+SF_6 →	27	[20]

Electron impact dissociation reactions of SF_6

Reaction	E_{th} (eV)	Rate coefficient (cm^3s^{-1})	Ref.
$e + SF_6 \rightarrow SF_5 + F + e$	9.6	$1.5 \times 10^{-7} e^{-5/T_e}$	
$e + SF_6 \rightarrow SF_4 + 2F + e$	12.4	$9 \times 10^{-9} e^{-13.4/T_e}$	
$e + SF_6 \rightarrow SF_3 + 3F + e$	16.0	$2.5 \times 10^{-8} e^{-33.5/T_e}$	
$e + SF_6 \rightarrow SF_2 + F_2 + 2F + e$	18.6	$2.3 \times 10^{-8} e^{-23.9/T_e}$	
$e + SF_5 \rightarrow SF_4 + F + e$	5.0	$1.46 \times 10^{-7} e^{-9.0/T_e}$	
$e + SF_4 \rightarrow SF_3 + F + e$	8.5	$6.2 \times 10^{-8} e^{-9.0/T_e}$	
$e + SF_3 \rightarrow SF_2 + F + e$	5.0	$8.6 \times 10^{-8} e^{-9.08/T_e}$	
$e + SF_2 \rightarrow SF + F + e$	8.0	$4.54 \times 10^{-8} e^{-9.0/T_e}$	
$e + SF \rightarrow S + F + e$	7.9	$6.2 \times 10^{-8} e^{-9.0/T_e}$	
$e + F_2 \rightarrow 2F + e$	1.6	$1.18 \times 10^{-8} e^{-5.77/T_e}$	

Electron impact ionization reactions of SF_6

Reaction	E_{th} (eV)	Rate coefficient (cm^3s^{-1})	Ref.
$e + SF_6 \rightarrow SF_5^+ + F + 2e$	16.0	$1.5 \times 10^{-7} e^{-5/T_e}$	
$e + SF_6 \rightarrow SF_4^+ + 2F + 2e$	20	$1.5 \times 10^{-7} e^{-5/T_e}$	
$e + SF_6 \rightarrow SF_3^+ + 3F + 2e$	20.5	$1.5 \times 10^{-7} e^{-5/T_e}$	
$e + SF_6 \rightarrow S^+ + F_2 + 4F + 2e$	18	$1.5 \times 10^{-7} e^{-5/T_e}$	
$e + SF_6 \rightarrow F^+ + SF_4 + F + 2e$	23	$1.5 \times 10^{-7} e^{-5/T_e}$	
$e + SF_5 \rightarrow SF_5^+ + 2e$	11	$1.5 \times 10^{-7} e^{-5/T_e}$	
$e + SF_5 \rightarrow SF_4^+ + F + 2e$	15	$1.5 \times 10^{-7} e^{-5/T_e}$	

Reaction	E_{th} (eV)	Rate coefficient (cm^3s^{-1})	Ref.

$e + SF_6 \rightarrow SF_5^+ + F + 2e$	16.0	$1.5 \times 10^{-7} e^{-5/T_e}$
$e + SF_6 \rightarrow SF_4^+ + 2F + 2e$	20	$1.5 \times 10^{-7} e^{-5/T_e}$
$e + SF_6 \rightarrow SF_3^+ + 3F + 2e$	20.5	$1.5 \times 10^{-7} e^{-5/T_e}$
$e + SF_6 \rightarrow S^+ + F_2 + 4F + 2e$	18	$1.5 \times 10^{-7} e^{-5/T_e}$
$e + SF_6 \rightarrow F^+ + SF_4 + F + 2e$	23	$1.5 \times 10^{-7} e^{-5/T_e}$
$e + SF_5 \rightarrow SF_5^+ + 2e$	11	$1.5 \times 10^{-7} e^{-5/T_e}$
$e + SF_5 \rightarrow SF_4^+ + F + 2e$	15	$1.5 \times 10^{-7} e^{-5/T_e}$

Reaction	E_{th} (eV)	Rate coefficient (cm^3s^{-1})	Ref.
$e + SF_6 \rightarrow SF_5^+ + F + 2e$	16.0	$1.5 \times 10^{-7} e^{-5/T_e}$	
$e + SF_6 \rightarrow SF_4^+ + 2F + 2e$	20	$1.5 \times 10^{-7} e^{-5/T_e}$	
$e + SF_6 \rightarrow SF_3^+ + 3F + 2e$	20.5	$1.5 \times 10^{-7} e^{-5/T_e}$	
$e + SF_6 \rightarrow S^+ + F_2 + 4F + 2e$	18	$1.5 \times 10^{-7} e^{-5/T_e}$	
$e + SF_6 \rightarrow F^+ + SF_4 + F + 2e$	23	$1.5 \times 10^{-7} e^{-5/T_e}$	
$e + SF_5 \rightarrow SF_5^+ + 2e$	11	$1.5 \times 10^{-7} e^{-5/T_e}$	
$e + SF_5 \rightarrow SF_4^+ + F + 2e$	15	$1.5 \times 10^{-7} e^{-5/T_e}$	

Reaction	E_{th} (eV)	Rate coefficient (cm^3s^{-1})	Ref.
$e + SF_6 \rightarrow SF_5^+ + F + 2e$	16.0	$1.5 \times 10^{-7} e^{-5/T_e}$	
$e + SF_6 \rightarrow SF_4^+ + 2F + 2e$	20	$1.5 \times 10^{-7} e^{-5/T_e}$	
$e + SF_6 \rightarrow SF_3^+ + 3F + 2e$	20.5	$1.5 \times 10^{-7} e^{-5/T_e}$	
$e + SF_6 \rightarrow S^+ + F_2 + 4F + 2e$	18	$1.5 \times 10^{-7} e^{-5/T_e}$	
$e + SF_6 \rightarrow F^+ + SF_4 + F + 2e$	23	$1.5 \times 10^{-7} e^{-5/T_e}$	
$e + SF_5 \rightarrow SF_5^+ + 2e$	11	$1.5 \times 10^{-7} e^{-5/T_e}$	

$e + SF_5 \rightarrow SF_4^+ + F + 2e$	15	$1.5 \times 10^{-7} e^{-5/T_e}$

Reaction	E_{th} (eV)	Rate coefficient (cm^3s^{-1})	Ref.
$e + SF_6 \rightarrow SF_5^+ + F + 2e$	16.0	$1.5 \times 10^{-7} e^{-5/T_e}$	
$e + SF_6 \rightarrow SF_4^+ + 2F + 2e$	20	$1.5 \times 10^{-7} e^{-5/T_e}$	
$e + SF_6 \rightarrow SF_3^+ + 3F + 2e$	20.5	$1.5 \times 10^{-7} e^{-5/T_e}$	
$e + SF_6 \rightarrow S^+ + F_2 + 4F + 2e$	18	$1.5 \times 10^{-7} e^{-5/T_e}$	
$e + SF_6 \rightarrow F^+ + SF_4 + F + 2e$	23	$1.5 \times 10^{-7} e^{-5/T_e}$	
$e + SF_5 \rightarrow SF_5^+ + 2e$	11	$1.5 \times 10^{-7} e^{-5/T_e}$	
$e + SF_5 \rightarrow SF_4^+ + F + 2e$	15	$1.5 \times 10^{-7} e^{-5/T_e}$	

Bibliography

1. G. Cunge, N. Sadeghi, and R. Ramos, J. Appl. Phys. 102, 093305 (2007).

2. R. Ramos, G. Cunge, O. Joubert, N. Sadeghi, M. Mori, and L. Vallier. (2007). *Thin Solid Films*, **515,** 4846–4852.

3. M. Fukasawa, A. Kawashima, N. Kuboi, H. Takagi, Y. Tanaka, H. Sakayori, K. Oshima, K. Nagahata, and T. Tatsumi. (2009). *Jpn. J. Appl. Phys.*, **48**, 08HC01.

4. H.K. Lee, K.H. Baek, and K. Shin. (2017). Jpn. J. Appl. Phys., 56, 066502.

5. J. V. Ringwood, S. Lynn, G. Bacelli, B. Ma, E. Ragnoli and S. McLoone. (2010). IEEE Trans. Semicond. Manuf., 23, 87-98.

6. S. Lynn, N. MacGearailt, J. V. Ringwood. (2012), J. Process Control, 22, 666-676

7. B. Keville, Y. Zhang, C. Gaman, A.M. Holohan, S. Daniels, and M.M. Turner. (2013). J. Vac. Sci. Technol. A, 31, 031302.

8. P. I. Klimecky, J. W. Grizzle and F. L. Terry. (2003). J. Vac. Sci. Tech. A, 21, 706.

9. S. Park, Y. Jang, S. Ryu, H.-J. Roh, and G.-H. Kim. (2015). IEEE Trans. Semicond. Manuf., 28(3), 241-246.

10. H.-J. Roh, S. Ryu, Y. Jang, N.-K. Kim, Y. Jin, S. Park, and G.-H. Kim. (2018). IEEE Trans. Semicond. Manuf. 31 (2), 232-241.

11. Y. Jang, H.-J. Roh, S. Park, S. Jeong, S. Ryu, J.-W. Kwon, N.-K. Kim, and G.-H. Kim. (2019) Curr. Appl. Phys. 19, 1068-1075.

12. U. Fantz. (2006). Plasma Sources Sci. Technol., 15, S137–S147.

13. J. T. Gudmundsson. (2001). Plasma Sources Sci. Technol., 10, 76.

14. S. Park, J.-M. Choe, H.-J. Roh, G.-H. Kim. (2014). J. Kor. Phys. Soc., 64 (12), 1819–1827.

15. J. B. Boffard, R. O. Jung, C. C. Lin, L. E. Aneskavich, and A. E. Wendt, J. Phys. D: Appl. Phys. 45 (2012) 045201.

16. D.V. Lopaev, A.V. Volynets, S.M. Zyryanov, A.L. Zotovich, and A.T. Rakhimov. (2017). J. Phys. D Appl. Phys., 50, 075202.
17. N. Skoro, N. Puac, S. Lazovic, U. Cvelbar, G. Kokkoris and E. Gogolides. (2013). J. Phys. D: Apply. Phys., 46, 475206.
18. M. A. Lieberman and A. J. Litchenberg. (2005). Principles of plasma discharges and materials processing, 2nd Ed., John Wiley & Sons.
19. PHELPS database (2013). http://www.lxcat.laplace.univ-tlse.fr.
20. Fortran program, MAGBOLTZ, S.F. Biagi, versions 8.9 and after.
21. P. Chabert and N. Braithwaite. (2011). Physics of Radio-Frequency Plasmas, Cambridge University Press.
22. J.-S. Kim, G.-H. Kim, T.-H. Chung, G.-Y Yeom and K.-H. Kwon (2001). J. Korean Phys. Soc. 38 (3) pp. 259-263.
23. D. E. Seborg, T.F. Edgar, D.A. Mellichamp and F.J. Doyle III (2011). “Process Dynamics and Control” 3rd Ed., Wiley Interscience.
24. I. L. Chien and P. S. Fruehauf (1990). Chemistry Engineering Progress, Vol. 86, No. 10, 1990, pp. 33-41.
25. L. G. Christophorou and J. K. Olthoff. (2000). J. of Phys. and Chem. Ref. Data 29, 267.
26. K. R. Ryan and I. C. Plumb (1989). Plasma Chem. and Plasma Processing, 10 (2). pp.207-229.

초 록

플라즈마 공정 기반의 반도체 및 디스플레이 제조 공정에서 공정 장비 상태 변동에 따른 공정 결과의 변동의 관리는 필수적이다. 공정의 미세화에 따라 예방 정비 (PM) 이후 혹은 공정 진행에 따른 공정 장비 상태의 경시 변화가 공정 수율에 미치는 영향은 커지고 있다. 공정 결과의 실측 데이터를 바탕으로 통계 알고리즘 기반 공정 제어가 (SPC) 주로 공정 관리에 활용되어왔으나, 공정 결과의 측정에 많은 시간과 비용이 소모되기 때문에 제어 주기가 웨이퍼 수 백장 단위로 매우 긴 단점이 존재한다. 보다 세밀한 공정 관리를 위해 매 웨이퍼마다 공정 계측, 제어가 필요하며 이를 위해 공정 결과의 가상 계측 (VM) 기술과 이를 바탕으로 매 공정마다 레시피를 수정하는 R2R 기술이 개발되었다. 그러나 플라즈마와 플라즈마 대면 부품 사이의 표면 반응에 의해 장비 상태는 공정 도중에도 실시간으로 변하고 있기 때문에 궁극적으로 초미세 공정 제어를 위해서는 실시간 공정 제어 기술이 필요하다.

본 연구에서는 반도체 및 디스플레이 제조 공정에서 가장 난이도가 높은 식각 공정을 대상으로 공정 진행 도중 공정 결과의 변동을 실시간으로 관측하는 PI-VM 기술을 개발하고, 장비 – 플라즈마 정보 (PI) 인자 – PI-VM의 2단 구조를 가지는 실시간 공정 제어기인 PI-APC 를 개발하였다. 플라즈마 공정은 반응기 내에서 전기장으로 인해 가속된 전자와 중성입자들 사이의 충돌 반응으로 인한 플라즈마의 생성과 생성된 플라즈마가 공정 타겟에 입사하여

발생하는 표면 반응으로 나누어진다. PI-VM으로 관측할 수 있는 공정 결과는 표면 반응이 시간에 따라 누적된 결과이며 광진단을 통해 관측할 수 있는 PI 인자는 장비 입력 값에 따른 동적 평형을 이루고 있기 때문에 실시간 공정 제어기는 장비 – PI 제어기와 PI – PI-VM 제어기 2단의 구조를 가져야 한다.

장비 – PI 제어기는 장비의 입력 값에 따른 플라즈마의 발생을 제어하기 때문에 전력 균형 방정식, 입자 균형 방정식 등을 통해 현상학적인 동적 모델을 바탕으로 개발할 수 있다. 제어기의 이득율은 장비 값 변동에 따른 PI 인자의 생성 반응과 소멸 반응의 비율로 나타나며, 제어기의 시상수는 장비의 동특성, 센서의 동특성, 플라즈마의 동특성 중 가장 느린 장비의 동특성을 따라간다.

PI – PI-VM 제어기는 단계적 변수 선택에 따른 다중 선형 회귀 (SVS-MLR) 알고리즘으로 개발된 PI-VM의 특성 인자와 가중치를 바탕으로 개발할 수 있다. 통상적인 VM과 다르게 PI-VM은 선형 회귀를 통해 공정 결과에 직접적으로 영향을 미치는 PI 인자의 영향력을 평가할 수 있기 때문에 PI-VM을 통해 제어기를 개발할 수 있었다. 공정 결과는 시간에 따른 표면 반응의 누적된 결과이기 때문에 SHMPC 방식을 사용하여 제어 결과를 동적 평형을 이루고 있는 PI 인자로 변환할 수 있으며, 제어 인자를 제외한 나머지 특성 인자에 의한 영향을 현상학적 모델을 기반으로 제거하여 선형 제어기화 할 수 있었다.

장비 – PI – PI-VM 구조의 PI-APC는 장비 상태 변동에 따른 식각 반응의 저하를 인지하고, 식각 반응 증진을 위한 불소 원자 생성을 산소 분자 유량으로 조절하였다. PI-APC는 첫 장 효과로 인한 식각

깊이의 12 % 변동을 공정 진행 중 실시간 제어를 통해 0.5 %까지 줄이는 성능을 보였다. 본 연구 결과를 통해 PI-APC는 In-wafer 제어가 공정 중 발생하는 플라즈마의 변동을 보상 제어하여, W2W 공정 결과 변동을 관리할 수 있음을 보였다. 또한 플라즈마 공정에 존재하는 비선형성을 현상학적 모델 기반의 2단 제어를 이용하여 선형화 하여 제어할 수 있음을 보였다. 따라서 PI-APC는 플라즈마 공정 내 존재하는 여러 동특성과 비선형성을 현상학적인 모델로 기술하여 공정의 경시 변동에 선행 대응하는 예지 정비 (PdM) 기술, 장비 간의 이격을 해소하는 TTTM 기술, 공정 레시피 최적화 기술 등을 개발하는데 활용될 수 있을 것으로 기대한다.

주요어: 플라즈마 정보 (PI) 인자, 가상 계측 (VM), 고급 공정 제어기 (APC), 플라즈마 식각, 첫 장 효과
학 번: 2013-23183